ARTICLE

Scheelite chemistry from skarn systems: implications for ore-forming processes and mineral exploration

Ana Carolina R. Miranda[1,2] · Georges Beaudoin[1,2] · Bertrand Rottier[1,2]

Abstract

The trace element composition of scheelite from 19 well-documented reduced and oxidized skarn systems was measured by laser ablation-inductively coupled plasma-mass spectrometry (LA-ICP-MS) to establish chemical criteria for the application of scheelite as an efficient indicator mineral for mineral exploration targeting. In both reduced and oxidized skarns systems, scheelite forms during prograde and retrograde stages. Prograde scheelite is texturally and chemically zoned, whereas retrograde scheelite is predominantly texturally homogeneous but may display chemical zonation. Five chondrite-normalized REE patterns, displaying both positive and negative Eu anomalies, are identified in the data: (i) steep and (ii) shallow negative slopes, (iii) concave, (iv) flat to slightly concave, and (v) convex shapes. The different REE patterns are related to variable fluid salinity and association with co-precipitated garnet or clinopyroxene. Results of partial least square-discriminate analysis (PLS-DA) show that scheelite composition varies according to skarn redox, intrusion composition, and metal association. These results support the fact that the trace element composition of scheelite is in part a function of igneous rock composition and oxygen fugacity, in addition to salinity, co-genetic minerals, and composition of the mineralizing fluids. Scheelite from reduced and oxidized skarns can be discriminated from those from orogenic and intrusion-related gold deposits due to their lower Sr and higher Mo, Ta, and Nb concentrations. Scheelite trace element composition investigated by PLS-DA is effective in discriminating different deposit types, supporting the use of scheelite as an indicator mineral for exploration targeting.

Keywords Scheelite · Trace element · Skarn systems · Indicator mineral · Partial least square-discriminant analysis

Introduction

Scheelite ($CaWO_4$) is a common tungsten ore mineral in skarn, greisen Sn, porphyry (Mo–W and Sn–W), and polymetallic deposits, as well as an accessory mineral in reduced intrusion-related gold systems (RIRGS), orogenic gold, Au skarns, and porphyry-skarn Cu deposits (Brown and Nesbitt 1987; Brugger et al. 1998, 2000; Uspensky et al. 1998; Hart 2007; Song et al. 2014; Guo et al. 2016; Fu et al. 2017; Poulin et al. 2018; Wintzer 2019; Xu et al. 2020; Sciuba et al.

2020). Because scheelite is a resistant mineral and occurs in several geological settings, it has been used as an indicator mineral for targeting primary tungsten bearing deposits (Toverud 1984; Averill 2001; McClenaghan et al. 2017) in addition to orogenic gold deposits (Uspensky et al. 1998; Maneglia et al. 2017; Grzela et al. 2019; Sciuba et al. 2020; de Bronac de Vazelhes et al. 2021).

The advances of micro analytical techniques (LA-ICP-MS) allow a wide range of trace elements in various minerals to be measured (Cook et al. 2016; Sylvester and Jackson 2016). Studies on mineral chemistry are essential to understand ore-forming processes, since the mineral trace element composition varies as a function of the origin, composition, and physicochemical conditions of hydrothermal fluids or melts from which it precipitates (Gaspar et al. 2008; Dare et al. 2012; Andersson et al. 2019; Mansur et al. 2021). Since the composition and physicochemical conditions of hydrothermal fluids are determined by the geological settings, and the chemical composition of minerals reflects this environment, the compositional

✉ Ana Carolina R. Miranda
  acrmiranda1@gmail.com

1 Département de Géologie et Génie Géologique, Université Laval, Québec, Canada

2 Centre de Recherche sur la Géologie et L'ingénierie de Ressources Minérales (E4m), Université Laval, Québec, Canada

variation of minerals is used to discriminate among magmatic or hydrothermal environments (Duran et al. 2016; Huang et al. 2019), deposit types (Dupuis and Beaudoin 2011; Boutroy et al. 2014; Dare et al. 2014; George et al. 2015a,b; O'Brien et al. 2015; Duran et al. 2016; Makvandi et al. 2016a, 2020; Mao et al. 2016; Gregory et al. 2019; Porter et al. 2020; Liu and Beaudoin 2021), hydrothermal alteration (Wilkinson et al. 2015), and mineralized and barren rocks (Gregory et al. 2019; Shu et al. 2019). Trace element chemistry of indicator minerals is used to vector toward ore bodies (Barker et al. 2020; Cook et al. 2020; Wilkinson et al. 2020; Rottier and Casanova 2020) and for exploration for diamonds (Gurney and Zweistra 1995; Grütter et al. 2004) and concealed deposits (Eppinger et al. 2011; Kelley et al., 2011; Duran et al. 2019). Several contributions have shown the potential use of scheelite chemistry for indicating different deposit types and the source of hydrothermal fluids (Ghaderi et al. 1999; Song et al 2014; Poulin et al. 2018; Sciuba et al. 2020).

Skarn deposits, where garnet and clinopyroxene are common minerals, are the main worldwide source of tungsten, and scheelite is one of the most common W ore minerals in these systems (Einaudi et al. 1981). Based on garnet and clinopyroxene major element compositions, skarns are classified following different redox states, reduced and oxidized, which is a result of magma and host rock compositions and depth of formation (Einaudi and Burt 1982; Newberry and Swanson, 1986; Meinert 1997; Chang et al. 2019). For instance, hedenbergitic clinopyroxene and grossular-spessartite garnet commonly occur in reduced skarns, whereas andradite garnet and diopsidic clinopyroxene are typically found in oxidized skarns (Einaudi et al. 1981; Einaudi and Burt 1982). Scheelite occurs in both redox skarn types and can be temporally and spatially associated with several other metals such as Au, Cu, Mo, and Sn (Lu et al. 2003; Hart 2007; Song et al. 2014). Therefore, scheelite chemistry may be used to target not only tungsten as the primary commodity, but also other metals (Au, Cu, Mo, and Sn) found in association with tungsten. Although scheelite major element chemistry has been studied in some detail (Raimbault et al. 1993; Ghaderi et al. 1999; Robert et al. 2006; Dostal et al. 2009; Song et al. 2014; Poulin et al. 2018; Zhao et al. 2018; Sciuba et al. 2020), its trace element composition remains poorly documented in several settings, and our understanding of the controls of its chemical composition and the application for the exploration for skarn deposits remains limited.

In this contribution, we document the chemical signature of scheelite, garnet, and clinopyroxene from various skarn systems to develop compositional fingerprints that allow discrimination of scheelite from reduced and oxidized skarns, skarn deposits with different metal associations, and other scheelite-bearing deposit types. The results are explored using basic and multivariate statistical methods, which establish chemical criteria for the scheelite as an efficient indicator mineral for mineral targeting.

Selected tungsten skarns deposits

Scheelite crystals and co-genetic minerals (garnet and clinopyroxene) from exoskarn samples from thirteen W($\pm$ Au–Cu–Mo–Sn) skarn deposits were investigated (Fig. 1; Table 1). Typical examples of scheelite-bearing skarn samples related to RIRGS (Scheelite Dome, Ray Gulch, Lermontovskoe and Vostok-2), Au skarn (Marn), and Cu-polymetallic porphyry-skarn deposit (Jiama) were also included in our dataset (Table 1). In total, scheelite-bearing skarn samples from 19 localities formed in varied geological settings, metal associations, from a range of deposit sizes, and mineralization ages ranging from Neoproterozoic to Miocene were selected (Table 1; Fig. 1).

According to Einaudi et al. (1981), scheelite skarns are classified in oxidized and reduced types, based on skarn mineralogy (Fe^{3+} versus Fe^{2+} bearing minerals, Fig. 2), which depends on the host rock composition, the redox state of the hydrothermal fluids, and on the depth skarn formation. In general, reduced skarns are hosted in pure limestone and are associated with ilmenite-series intrusions (Ishihara 1977), emplaced at greater depth (> 2 kbar) relative to, for example, skarns associated with porphyry Cu systems (Newberry and Swanson 1986; Chang et al. 2019). In contrast, oxidized skarns are closely associated with magnetite-series intrusions emplaced at shallow crustal levels (< 2 kbar; Newberry 1983; Newberry and Swanson 1986; Chang et al. 2019) and developed in impure carbonates and/or hematite-rich metasedimentary host rocks (Newberry 1983; Newberry and Swanson 1986).

Newberry (1983) and Zaw and Singoyi (2000) showed that scheelite skarns might also be classified as moderately reduced (e.g., Pine Creek, California) to moderately oxidized (e.g., King Island, Tasmania) because they show intermediate characteristics between end-member of oxidation state, host rock composition, and depth of formation (Kwak and Tan 1981; Newberry 1983). For simplicity, in this study we grouped the moderately oxidized skarns with oxidized, and moderately reduced with reduced skarns, respectively (Table 1). Typical examples of reduced scheelite-bearing skarns include Sangdong (South Korea) and Cantung and Mactung (Canada), whereas Kara (Australia) and Costabonne (France) are examples of oxidized W skarns (Einaudi et al. 1981; Dick and Hodgson 1982; Zaw and Singoyi 2000; Table 1).

The reduced skarn prograde mineral assemblage is dominated by hedenbergitic (Fe^{2+}-rich) clinopyroxene over grossular-spessartite (Al-rich) garnet (Fig. 2). The retrograde assemblage comprises hornblende and/or biotite, and
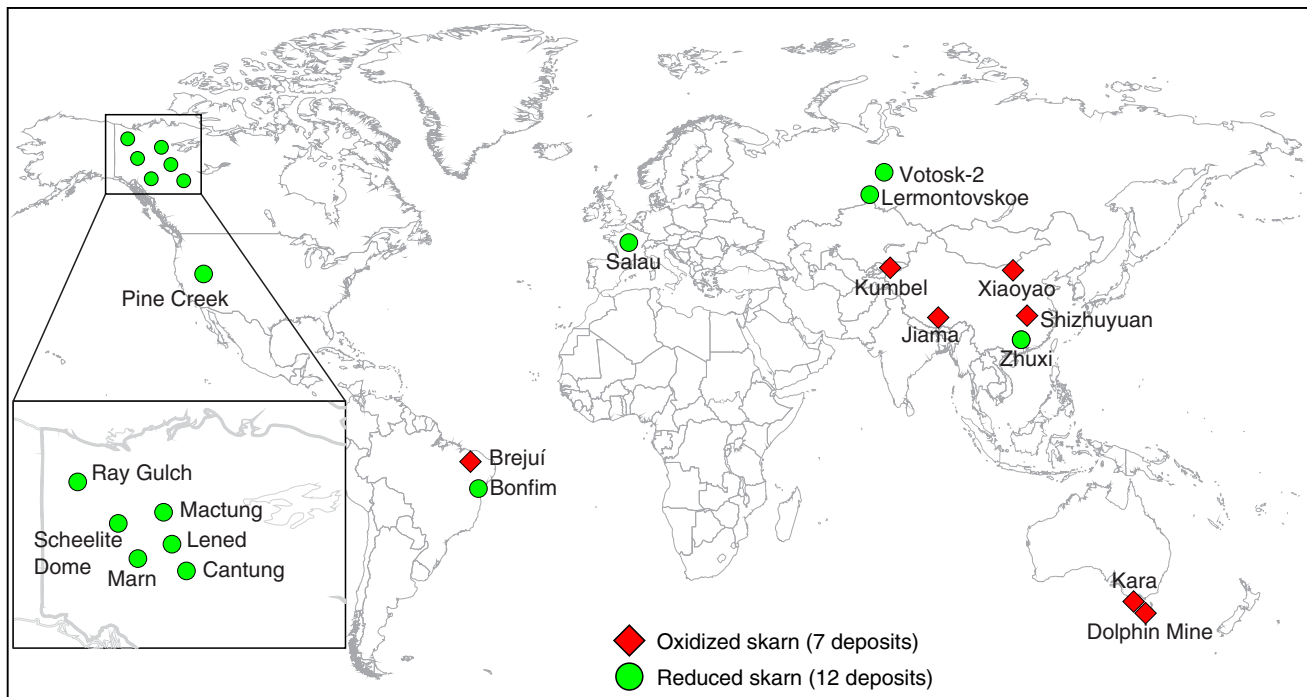
Fig. 1 World distribution of sampled scheelite-bearing skarn deposits (references included in Table 1)

sulfides such as pyrrhotite, chalcopyrite, molybdenite, sphalerite, and arsenopyrite (Dick and Hodgson 1982; Mathieson and Clark 1984). In oxidized skarns, andradite (Fe^{3+}-rich) garnet is more abundant than diopisidic clinopyroxene in the prograde stage (Fig. 2), whereas the retrograde assemblage consists mainly of epidote, hornblende, magnetite, and pyrite (Kwak and Tan 1981; Zaw and Singoyi 2000). In both redox type skarns, fine-grained, Mo-rich (> 1000 ppm) scheelite occurs in the prograde stage, whereas coarse-grained, Mo-poor (< 1000 ppm) scheelite occurs commonly in the retrograde stage (Kwak and Tan 1981; Liu et al. 2020; Su et al. 2020).

Methodology

Sample selection

Fifty-three scheelite-bearing skarn samples from 19 well-documented deposits distributed worldwide were investigated (Fig. 1 and Table 1). Garnet and clinopyroxene compositions from literature and this study were used as proxies for redox conditions (ESM1 Table S1; Fig. 2). Twelve are classified as reduced, and 7 as oxidized skarns (Table 1, Fig. 2). In total, 70 polished thin sections were studied to constrain mineralogy, morphology, texture, and chemical composition of scheelite and co-existing minerals in different skarn facies.

Electron probe micro-analyses (EPMA) and cathodoluminescence images (CL)

Major and minor element composition of scheelite ($n = 164$ analysis), garnet ($n = 84$) and clinopyroxene ($n = 32$) (ESM1 Table S1), and cathodoluminescence (CL) images of scheelite were obtained by electron probe micro-analyser (EPMA) at Université Laval, using a CAMECA SX-100 instrument equipped with five wavelength-dispersive spectrometers (WDS) and a CL detector. The analyses were performed using a 10-µm-diameter beam. Analytical conditions for major elements analyses were 20 nA for beam current and 15 kV for accelerating voltage, with a counting time of 20 s at the peak and 10 s at the background. For minor elements in scheelite (Na, Sr, Mo, Y, and Fe), the analytical conditions were 100-nA beam current, 15 kV of accelerating voltage, and counting times of 120 s at the peak and 30 s at the background. Metal tungsten (W), metal molybdenum (Mo), MgO (Mg), diopside (Ca), quartz (Si), celestite (Sr), YPO_4 (Y), magnetite (Fe), albite (Na), plagioclase (Al), rutile (Ti), Cr (chromite), sphalerite (Zn), rhodochrosite (Mn), zircon (Zr), apatite (P), and orthoclase (K) were used as standards. For CL investigation, the accelerating voltage was set at 15 kV, the beam current at 20 nA, and work distance fixed at 2 mm. The dwell time of each pixel was 0.03 ms. The CL images were recorded in gray scale in order to document texture and zonation patterns in scheelite prior to other micro-analyses.

Table 1 Summary of the main geological characteristics of scheelite-bearing skarn samples

Deposit/Country	Metal association	Host rocks	Intrusive rocks	Alumina Saturation Index (ASI) and redox state of intrusive rocks	Skarn facies	Garnet compoment (mole %)*	Clinopyroxene component (mole %)*	Skarn type	Tonnage and grade	Temperature**	Salinity (wt.% NaCl)	Reference
Tungsten skarn deposits												
Shizhuyuan/China	W-Mo-Sn-Bi-F	Devonian limestone	Jurassic biotite Kfeldspar granodiorite	peraluminous, magnetite-series	grt, amph	Ad15-76	Hd10-47	Oxidized	0.8 Mt WO3, 0.3% W, 0.5 m.t. Sn (metal), 0.2 m.t. Bi (metal), 0.1 m.t. Mo (metal)	350 - 535°C	26 - 41	Mao et al. (1996); Lu et al. (2003)
Kumbel/Kyrgyzstan	W-Mo-Cu-Bi	Devonian and Carboniferous sandy limestones and sandstones	Carboniferous monzogabbro–monzonite–granodiorite–granite pluton	magnetite-series	grt	Ad40-98	Hd0-22	Oxidized	10 Mt, 17 000 t of WO3, (0.4% WO3); 100000 t Cu (0.25% Cu); 2500 t Bi (0.02% Bi); 500 t Mo (0.05 % Mo)	120 - 600°C	18 - 60	Soloviev (2015)
Xiaoyao/China	W-Mo-Cu	Cambrian limestone	Jurassic granodiorite	metaluminous, magnetite-series	grt	Ad78-100	-	Oxidized	50000t of WO3, 0.2% WO3, 6700t Cu, 360t Mo	-	-	Su et al. (2020)
Brejui/Brazil	W	Neoproterozoic marble and gneiss	Neoproterozoic biotite granite	-	grt, mag	Ad19-49	Hd30-60	Oxidized	17 Mt, 0.5-1% WO3	200 - 550°C	<15	Souza Neto et al. (2008)
Kara/Australia	Fe-W	Ordovician limestone	Denovian highly fractionated granite	peraluminous, magnetite-series	grt, mag	Ad70-100	Hd0-25	Oxidized	0.4 Mt, 0.75% WO3	240 - 600°C	2 - 45	Zaw and Sinogyi (2000); Sinogyi and Zaw (2001)

Table 1 (continued)

Deposit/Country	Metal association	Host rocks	Intrusive rocks	Alumina Saturantion Index (ASI) and redox state of intusive rocks	Skarn facies	Garnet compoment (mole %)*	Clinopyroxene component (mole %)*	Skarn type	Tonnage and grade	Temperature**	Salinity (wt.% NaCl)	Reference
King Island/Australia	W	Cambrian dolomite	Devonian mozogranite to granodiorite	magnetite-series	grt-px	Ad43-98	Hd23-98	Oxidized	9.6 Mt, 0.9% WO3	180 - 800°C	3 - 65	Kwak and Tan (1981)
Pine Creek/USA	W	Cambrian carbonate-rich metasedimentary rocks	Cretaceous quartz monzonite	titanite-bearing granite	px-grt	Ad30-65	Hd47-80	Reduced	16 Mt, 0.5% WO3	350 - 550°C	-	Newberry (1982); Porter (2013)
Zhuxi/China	W-Cu	Carboniferous carbonaceous shales and limestones	Mesozoic biotite granite	peraluminous, ilmenite-series	grt-wo, amph	Ad7-15	-	Reduced	6.37 Mt, 0.54% WO3, 0.57% Cu	280 - 500 °C	1.6 - 6.0 (few with 60)	Pan et al. (2018,2020)
Lened/Canada	W-Cu	Cambrian limestone	Cretaceous biotite quartz monzonite	peraluminous, ilmenite-series	grt, px, amph, po-bt	Ad20-40	Hd55-98	Reduced	0.7 Mt, 1% WO3, 0.15% Cu	-	-	Dick and Hodgson (1982); Marshall et al. (2004)
Cantung/Canada	W-Cu	Cambrian limestone	Cretaceous biotite granite and biotiterich dikes	peraluminous, ilmenite-series	px-grt, amph, po	Ad30-49	Hd75-99	Reduced	E-zone: 0.77 Mt, 1.75% WO3; Open pit: 3.4 Mt, 0.55% WO3	270 - 520 °C	4 - 14	Dick and Hodgson (1982); Mathieson and Clark (1984)
Mactung/Canada	W-Cu	Cambrian limestone	Cretaceous biotite granite	peraluminous, ilmenite-series	px, po	Ad15-20	Hd40-83	Reduced	33 Mt, 0.88% WO3	350 - 470 °C	<5	Dick and Hodgson (1982)
Salau/France	W-Au	Ordovician carbonate rocks	Variscan granodiorite	ilmenite-series	grt, po	Ad7-14	Hd35-97	Reduced	0.01 Mt, 1.44% WO3, 2 g/t Au	-	-	Poitrenaud et al. (2019)

Table 1 (continued)

Deposit/Country	Metal association	Host rocks	Intrusive rocks	Alumina Saturation Index (ASI) and redox state of intrusive rocks	Skarn facies	Garnet compoment (mole %)*	Clinopyroxene compoment (mole %)*	Skarn type	Tonnage and grade	Temperature**	Salinity (wt.% NaCl)	Reference
Bonfim/Brazil	W-Au	Neoproterozoic marble and schist	Neoproterozoic biotite granite		px	-	Hd17-53	Reduced	>0.3 Mt, 4.8 % WO3, 0.5-1.5 t Au	400 - 580 °C	4.8	Souza Neto et al. (2008)
Tungsten skarns associated with RIRGS												
Ray Gulch or Mar or Wolf/Canada	W	Proterozoic-Early Cambrian Quartzbiotite schist and carbonate	Cretaceous granodiorite	metaluminous, titanite-bearing granite	px	-	Hd60-92	Reduced	12.6 Mt at 0.31 % WO3	-	-	Brown et al. (2002)
Vostok-2/Russia	W-Cu(Au)	Paleozoic limestone	Cretaceous granodiorite	peraluminous, ilmenite-series	po, bt	Ad10-25	Hd25-80	Reduced	180 Kt WO3 and 10 - 15 t Au, averaging 1.7% WO3, 0.64% Cu, and 1.9 g/t Au	420 - 460 °C	5.4 - 12	Soloviev et al. (2017)
Lermontovskoe/Russia	W-Cu(Au)	Paleozoic limestone	Cretaceous granodiorite-granite	peraluminous, ilmenite-series	po, bt	-	Hd70-90	Reduced	0.048 Mt, 2.6% WO3, 0.23 g/t Au	360 - 500 °C	low salinity	Soloviev et al. (2015)
Scheelite Dome/Canada	Au-W	Proterozoic-Cambrian marble	Cretaceous quartz monzonite to granodiorite	metaluminous, titanite-bearing granite	px-po	-	Hd80-90	Reduced	Drilling in 1979 intersected 1.5 m grading 0.35% WO3 and 1.2 g/t Au	300 - 500 °C	4	Meinert et al. (2005); Mair et al. (2006)

Table 1 (continued)

Deposit/Country	Metal association	Host rocks	Intrusive rocks	Alumina Saturation Index (ASI) and redox state of intrusive rocks	Skarn facies	Garnet compoment (mole %)*	Clinopyroxene component (mole %)*	Skarn type	Tonnage and grade	Temperature**	Salinity (wt.% NaCl)	Reference
Gold skarn												
Marn/Canada	Au-Cu-W	Permin sedimentary and limestone	Cretaceous monzonite	metaluminous, magnetite-series	px-po	-	Hd80-100	Reduced	0.3 Mt, 8.6 g/t Au, 1% Cu, 0.1% WO3 and 17 g/t Ag	-	-	Brown and Nesbitt (1987)
Cu porphyry-skarn system												
Jiama/China	Cu-polymetallic	Jurassic limestone	Miocene granitegranodiorite porphyries	metaluminous, magnetite-series	grt, qtz, cc	Ad60-100	Hd0-20	Oxidized	7.4 Mt Cu, 0.6 Mt Mo, 1.8 Mt Pb+Zn, 6.65 Moz Au, 350.32 Moz Ag	225 - 550 °C	<36.2	Zheng et al. (2016)

* Garnet and clinopyroxene EPMA analysis from this study and literature

** Temperature range of prograde and retrograde stages
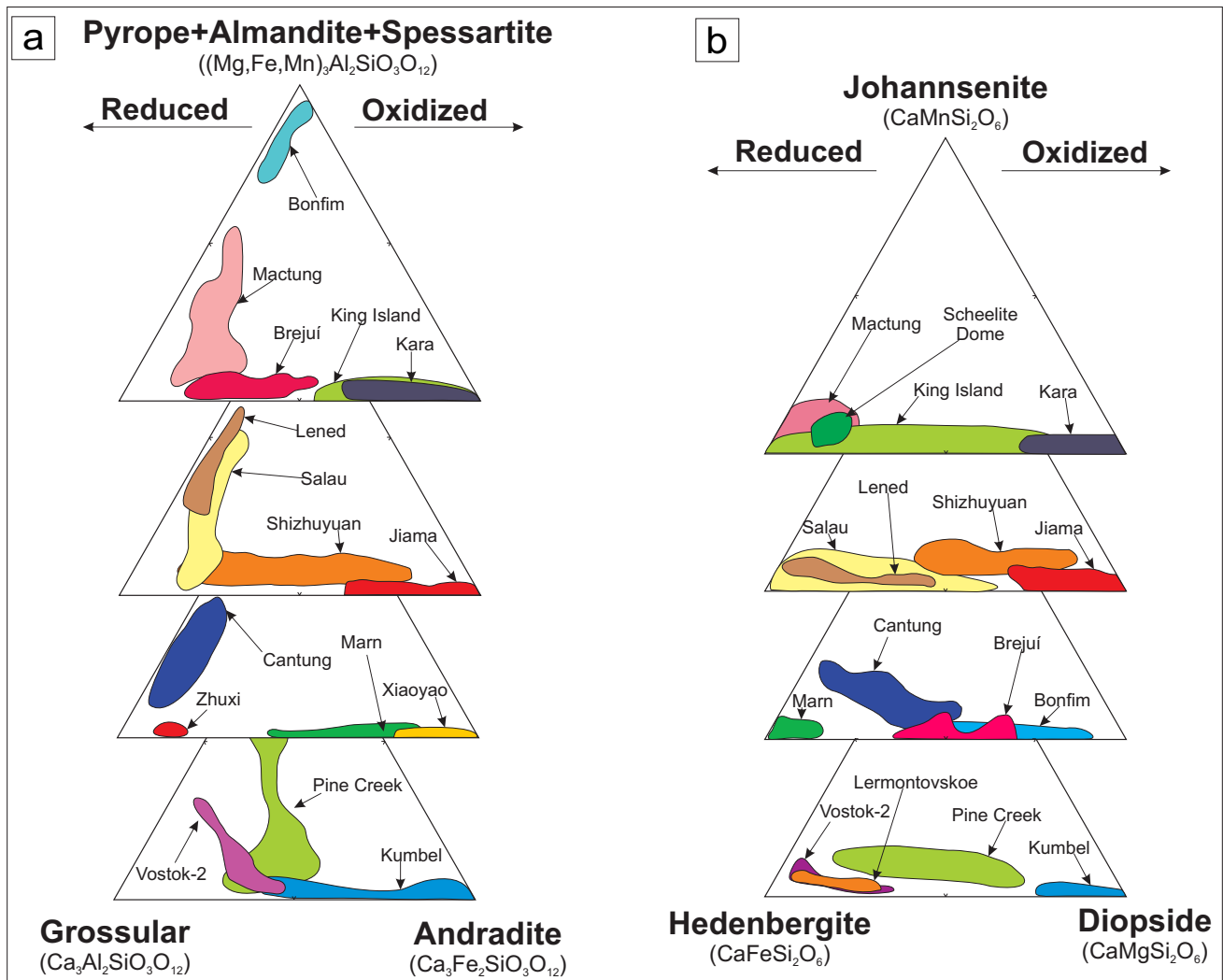
Fig. 2 Ternary diagrams for garnet (**a**) and clinopyroxene (**b**) compositional variations from the studied scheelite-bearing skarn deposits. Data from literature (references included in Table 1) and this study (ESM1 Table S1)

Laser ablation-inductively coupled plasma-mass spectrometry (LA-ICP-MS)

The concentration and distribution of the minor and trace element in scheelite ($n = 382$), and in garnet ($n = 32$), and clinopyroxene ($n = 31$), were determined by LA-ICP-MS at the LabMaTer, Université du Québec à Chicoutimi (UQAC), using an Excimer 193 nm RESOlution M-50 laser ablation system (Australian Scientific Instrument) equipped with a double volume cell S-155 (Laurin Technic) and coupled with an Agilent 7900 mass spectrometer. The LA-ICP-MS tuning parameters were a laser frequency of 15 Hz, a fluence of 3 J/cm^2, and rastering speed of 10 μm/s for the line scans. Spots and line scans across the surface of scheelite grains were made with beam sizes of 33 and 55 μm, depending on grain size. Given the distinct textures in scheelite, the spots were performed in all distinct CL zones to obtain most variance as

possible in scheelite composition. For garnet and clinopyroxene, spot analyses were made with beam size of 55 μm. Data reduction was carried out using the Iolite v3 running in Igor Pro 6.37 (Paton et al. 2011). The ^{44}Ca was used for internal standardization for scheelite and silicates, based on EPMA results (ESM1 Table S1). Synthetic glass reference material NIST-610 were used as external standard for all elements using preferred values from the GeoReM database (Jochum et al. 2005). In addition, GSE-1 g, GSD-1 g, and Gprobe6-A, which are basalt glasses, and NIST-612, which is a synthetic glass, were used as secondary reference materials for quality control. They were analyzed at the beginning, throughout and the end of each analytical session, to monitor a potential instrumental drift. The following isotopes were measured: ^{11}B, ^{23}Na, ^{24}Mg, ^{39}K, ^{44}Ca, ^{49}Ti, ^{51}V, ^{55}Mn, ^{57}Fe, ^{59}Co, ^{61}Ni, ^{63}Cu, ^{66}Zn, ^{75}As, ^{85}Rb, ^{88}Sr, ^{89}Y, ^{93}Nb, ^{95}Mo, ^{137}Ba, ^{139}La, ^{140}Ce, ^{141}Pr, ^{146}Nd, ^{147}Sm, ^{153}Eu, ^{157}Gd, ^{159}Tb, ^{163}Dy,

^{165}Ho, ^{166}Er, ^{169}Tm, ^{172}Yb, ^{175}Lu, ^{181}Ta, ^{182}W, ^{183}W, ^{208}Pb, ^{209}Bi, ^{232}Th, and ^{238}U. Silicon and S were also monitored to identify possible silicate and sulfide inclusions, respectively. Analyses affected by inclusions were discarded.

Maps of element distribution of individual scheelite grain used a laser frequency of 15 Hz and power of 3 mJ/pluse. Different beam size (19 and 25 μm) and stage movement speed (10 to 20 μm/s) were used to optimize spatial resolution according to grain size. The maps were generated using Iolite v3 based on the time-resolved composition of each element. The maps indicate the relative concentration of the elements and are semi-quantitative. Detailed information about laser setting and results for reference material are presented in ESM1 Tables S2 and S3, respectively.

Statistical analysis

Scheelite compositional data were investigated using basic and multivariate statistics using Rstudio v4.04 (R Core Team 2021). Elements with ≤ 40% below detection limit (bdl) or left-censored data were imputed using log-ratio Expectation–Maximization (lrEM) algorithm from the R package zCompositions (Palarea-Albaladejo and Martín-Fernández 2015). The lrEM algorithm replaces left-censored values by expected values conditional to the information provided by the compositional dataset (Palarea-Albaladejo and Martín-Fernández 2013, 2015). Elements with over 40% left-censored data were excluded from further analysis. After imputation, the dataset was transformed using centered-log ratios (clr) to overcome the closure effect in compositional data (Aitchison, 1986). The clr-transformed values were investigated using partial least squares-discriminant analysis (PLS-DA, mixOmics package in R) to reveal hidden correlations among elements, and to identify potential elements useful to classify scheelite from different geological settings.

The PLS-DA is a supervised method that combines linear regression with classification technique. It consists of making a regression model from a predictive matrix X (variables/elements) to a response matrix Y (known groups/samples). To separate the known groups, the model finds the maximum covariance of uncorrelated linear transformations (latent components) of X and Y matrices, and the variables that best describe their differences. The results are visualized on scatter plots referred to as loading and scores plots (Makvandi et al. 2016b), and in bar plots referred to as scores contribution and as variable importance on projection (VIP) (Makvandi et al. 2016b). The loadings plot displays the correlations among the variables and illustrates the relationship between variables and groups. Variables that plot in the same quadrant are positively correlated, whereas those plotting on opposite quadrants are negatively correlated. Additionally, the farther an element plots from the origin of the diagram, the greater its contribution to the model. The scores plot displays the distribution of the samples and the relationship among the groups, where samples with similar features are grouped together (Eriksson et al. 2001). The score contribution plot is used to highlight the differences between each group and the average of the entire dataset. In compositional data, the element contribution reflects its concentration. The VIP plot emphasizes the importance of each element for the model. Elements with VIP values ≥ 1 have major controls in the discriminant analysis, whereas those between 0.8 and 1, and < 0.8 have intermediate and minor contributions to the model, respectively (Eriksson et al. 2001).

Results

Texture and scheelite composition

In oxidized and reduced skarns, scheelite associated with prograde assemblages is commonly fine grained (< 1 mm) and varies from rounded to euhedral, occurring as inclusions within garnet, less commonly within clinopyroxene, and as disseminated crystals (Fig. 3a–c). Scheelite associated with retrograde stages varies from fine- to coarse-grained (from 1 to 5 mm), rounded to euhedral and is mostly disseminated (Fig. 3d–f). Mineral inclusions such as amphibole, biotite, pyrrhotite, apatite in reduced skarns, and magnetite in oxidized skarns, are commonly found in scheelite, especially in retrograde stages (Fig. 3e–f).

Cathodoluminescence (CL) and backscatter electron (BSE) photomicrographs reveal three different internal textures in scheelite: (i) homogeneous, (ii) zoning, and (iii) dissolution fronts (Fig. 4). Homogenous scheelite is commonly associated with retrograde stages, and less often with prograde stages (Fig. 4a–b), whereas zoned scheelite commonly occurs in prograde stages (Fig. 4c–f). Two zoning patterns were identified: (i) oscillatory and (ii) patchy. Oscillatory zoning is the most common and is characterized by alternation of darker- and lighter-gray micrometric bands (Fig. 4c–d). Patchy zoning is less common and consists of irregular zones (Fig. 4e). Dissolution fronts are observed in zoned (Fig. 4e–f) and in homogenous crystals (Fig. 4b), and are characterized by resorption/dissolution of external parts of scheelite crystals, leading to variably rounded shapes with overgrown rims.

Compositional data for scheelite and ΣREE for garnet and clinopyroxene are reported in supplementary data (ESM1 Tables S4 and S5). In scheelite, Mo is the only trace element with median concentration above 100 ppm. Cerium, Sr, Nd, Nb, La, Y, Mn, and Na have median concentrations between 10 and 100 ppm, whereas B, Mg, K, As, Pr, Sm, Eu, Gd, Dy, Er, Yb, and Pb have median contents between 1 and 10 ppm. Titanium, V, Co, Ni, Ba, Tb, Ho, Tm, Lu, Ta, Bi, Th, and U have the lowest median concentrations, which

Fig. 3 Photomicrographs under transmitted light **a–d** and reflected light **e-f** of scheelite-bearing skarn samples. **a.** Scheelite associated with garnet (King Island). Scheelite occurs as inclusions in andradite, and as disseminated grains in the matrix. **b.** Scheelite inclusions in garnet from garnet-clinopyroxene skarn facies (Lened). **c**. Scheelite associated with clinopyroxene (Mactung). **d**. Disseminated scheelite associated with amphibole (Cantung). **e**. Scheelite grains associated with magnetite and amphibole from magnetite skarn (Kara). **f**. Scheelite with pyrrhotite, biotite, and chalcopyrite (Lened). Note biotite and pyrrhotite inclusions close to scheelite grain boundaries. sch: scheelite; grt: garnet; cpx; clinopyroxene; qz: quartz; mag: magnetite; amph: amphibole
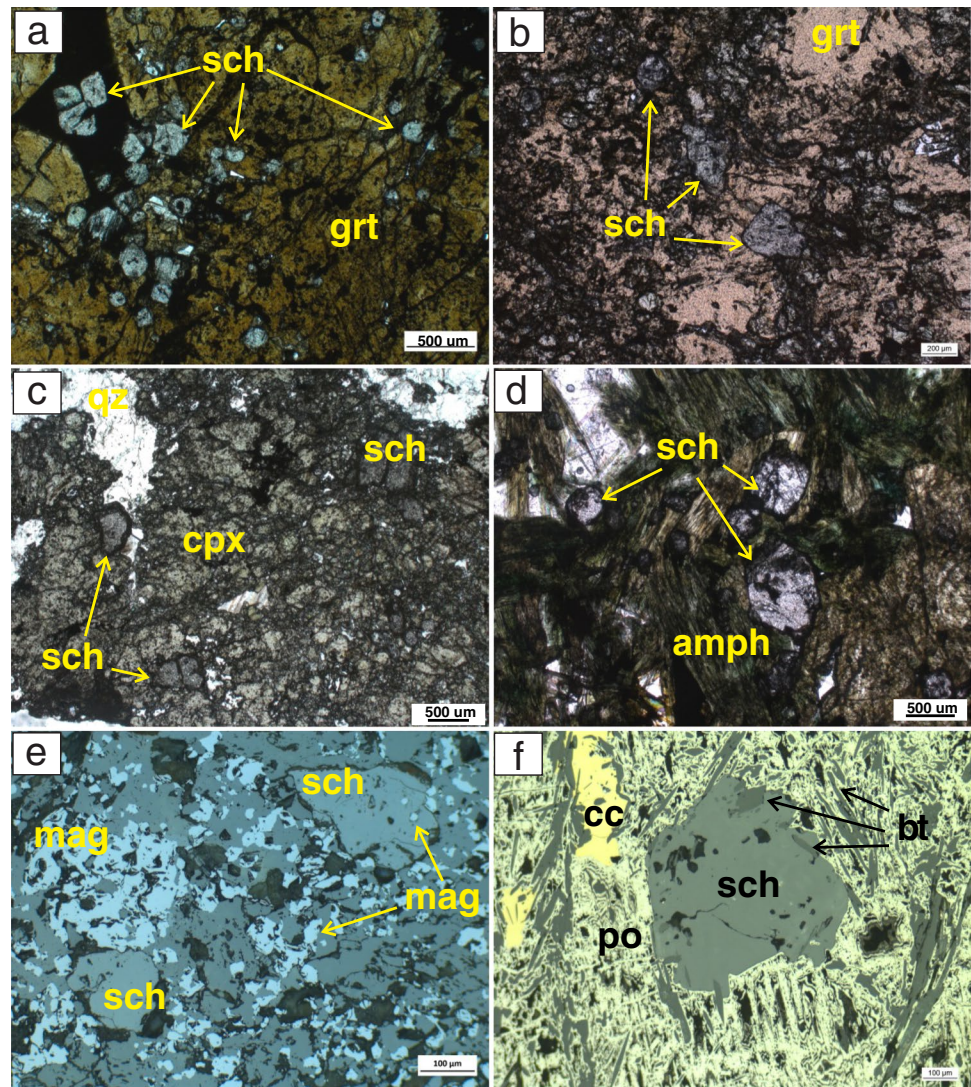
are all below 1 ppm. The concentration ranges for each element are shown in box and whisker plot grouped according to skarn redox (Fig. 5).

Trace element concentrations of scheelite from oxidized and reduced skarns show significant differences (Fig. 5). Scheelite from oxidized skarns has higher concentrations of Mo (< 18.1 wt.%), As (< 103 ppm), Ti (< 42 ppm), V (< 16 ppm), and Pb (< 52 ppm) compared to those from reduced skarns (Mo < 7 wt.%, As < 27 ppm, Ti < 28 ppm, V < 3 ppm, and Pb < 18 ppm; Fig. 5). Yttrium, Nb, Ta, and HREE display higher contents in reduced skarn scheelite (Y < 1980 ppm, Nb < 970 ppm, Ta < 11, and HREE < 1450 ppm; Fig. 5) and lower concentrations in oxidized skarn scheelite (Y < 197 ppm, Nb < 77 ppm, Ta < 2, and HREE < 206 ppm; Fig. 5). Boron, K, Sr, Na, Mg, Co, Ni, Mn, Ba, LREE, Th, and U have similar concentration ranges in scheelite from both skarn types (Fig. 5). Given

these differences, scheelite from oxidized skarns has higher LREE/HREE (up to 510) and Mo/Nb (from 5 to 40,577) ratios relative to reduced skarn scheelite (LREE/HREE from 0.6 and 65, and Mo/Nb < 324; Fig. 6a–b). Significant positive correlations exist between ΣREE-Eu + Y and Na, As + V, and Nb + Ta (Fig. 6c–e) in both reduced and oxidized skarns scheelite. The MoO_3 and WO_3 contents are negatively correlated (Fig. 6f). Weak to no correlations are noticed between U and Mo (Fig. 6g), ΣREE-Eu + Y, and K (ESM2 Fig. S1a) in reduced and oxidized skarns. Europium anomaly and Mo display a weak negative correlation in reduced skarn scheelite, and no correlation in oxidized skarns (Fig. 6h). A positive correlation is observed between U and Th in scheelite from both reduced and oxidized skarns (Fig. 6i).

Figure ESM2 S2 and Fig. 7 show representative LA-ICP-MS multielement maps of scheelite grains found in (i) prograde stage oxidized tungsten skarn (King Island; ESM2 Fig. S2) and (ii) retrograde stage from reduced tungsten skarn

Fig. 4 Cathodoluminescence (**a–b, d–f**) and backscattered electron (**c**) images of scheelite crystals. **a**. Homogeneous scheelite from Zhuxi. **b**. Homogeneous scheelite cut by late, brighter CL scheelite (Kara). **c**. and **d**. scheelite with oscillatory zoning from King Island and Jiama, respectively. **e.** Scheelite with irregular zoning and with an overgrown of brighter CL scheelite (Mactung). **f**. Scheelite with narrow oscillatory zoning with an overgrown of brighter CL scheelite (Mactung)
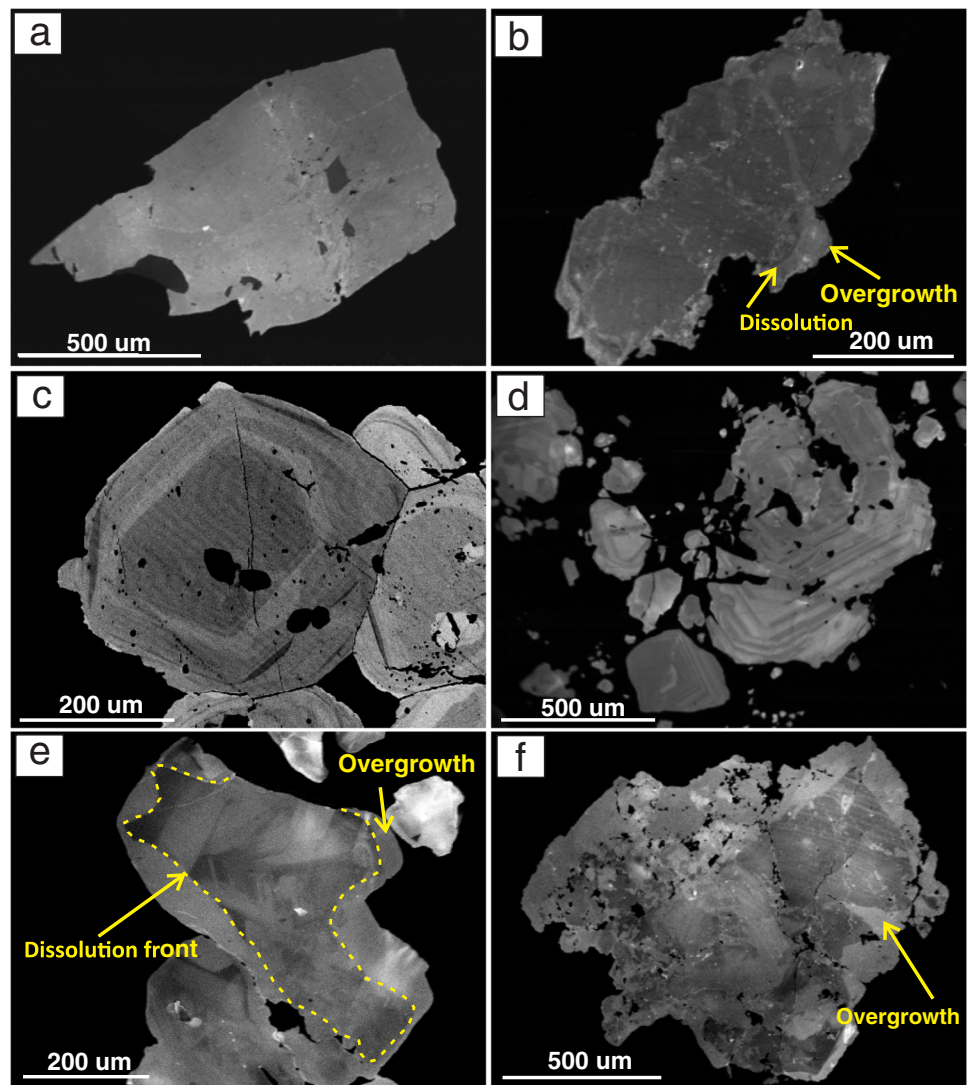
(Cantung; Fig. 7). The maps revel that Mo is the main element mirroring the CL zoning in scheelite. The CL-darker domains coincide with Mo-rich bands, and the lighter domains represent Mo-poor sectors (ESM2 Fig. S2 and Fig. 7). In contrast, more homogenous grains display flat Mo signal (Fig. 8). Some of the darkest CL zones coincide with high Nb, U, and Th concentrations (ESM2 Fig. S2 and Fig. 7). Strontium, As, Y, and ΣREE distributions do not correlate with the internal textures revealed by CL imaging, even though these elements also show a heterogeneous distribution in the elemental maps. Strontium varies from zoned (ESM2 Fig. S2 and Fig. 7) to homogenous (Fig. 8c–d). Arsenic exhibits a zoned distribution in scheelite from oxidized skarn, which roughly matches the Mo zonation (ESM2 Fig. S2). However, it tends to be more homogenously distributed in scheelite from reduced skarns (Figs. 7 and 8c), and in unzoned scheelite from oxidized retrograde skarns (Fig. 8d). Yttrium and Yb have a similar distribution and differ from that of Eu and La (ESM2 Fig. S2

and Fig. 7). Cores of zoned crystals are depleted in Y and Yb relative to the younger rims. In contrast, La is higher in the core relative to the rims (ESM2 Fig. S2; Figs. 7 and 8c–d), whereas Eu displays variable distribution relative to La and Y.

Garnet and clinopyroxene composition

Figure 2 shows a compilation of major elements composition of garnet and pyroxene from this study and literature (Table 1 for references). These data show that garnet from reduced skarn varies in composition mostly from grossular to spessartite ($Gr_{88}Ad_{12}Sp_0$–$Gr_{63}Ad_{10}Sp_{27}$), whereas in oxidized skarns garnet composition ranges from andradite to grossular ($Gr_0Ad_{100}Sp_0$–$Gr_{20}Ad_{80}Sp_0$), but being predominantly andraditic in composition (> 50% mol of andradite). Clinopyroxene was analyzed for major and trace elements only in reduced skarns, since it is rare in oxidized skarns. Clinopyroxene from reduced skarns varies
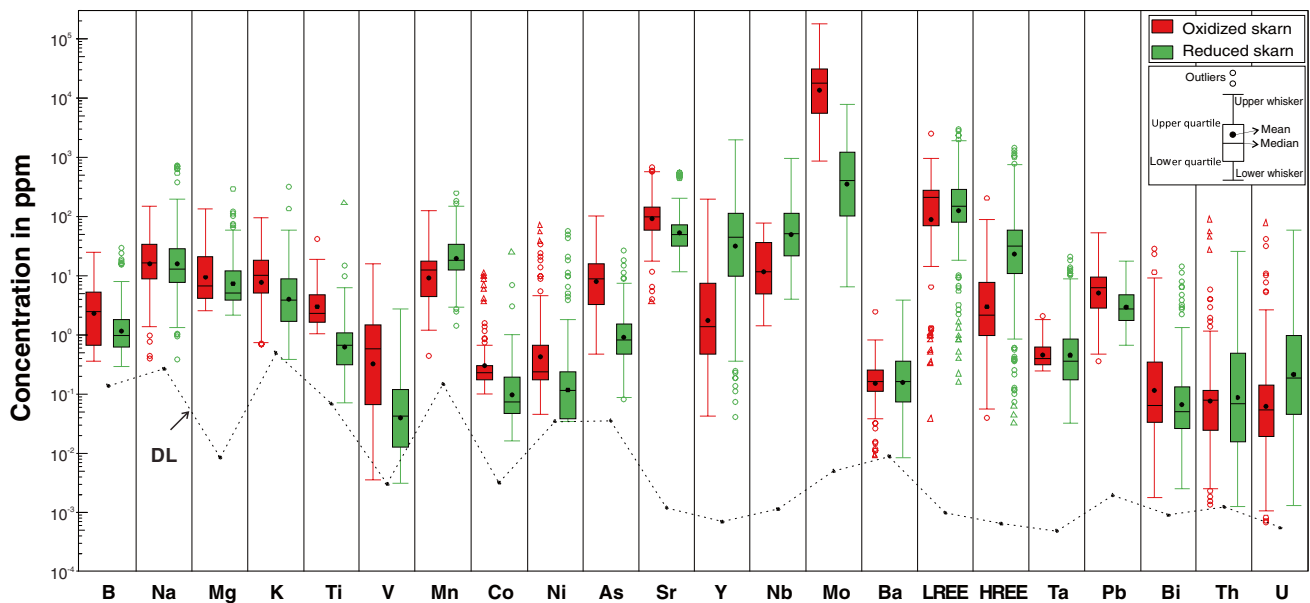
Fig. 5 Box and whisker diagram of trace elements concentrations in scheelite from reduced and oxidized skarns. Dashed line represents the detection limit (DL). Note that scheelite from oxidized skarns contains higher concentrations of Ti, V, As, and Mo, whereas scheelite from reduced skarns contains higher concentrations of Nb, Y, and HREE

in composition from diopside to dominantly hedenbergite (Fig. 2; $Di_{80}Hd_{18}Jo_2$–$Di_8Hd_{88}Jo_4$).

Garnet and clinopyroxene have much lower ΣREE content compared to scheelite. In garnet, ΣREE contents vary from 0.01 to 134.5 ppm, whereas in clinopyroxene these vary from 0.2 to 8.8 ppm (ESM1 Table S5). Grossular-spessartite garnet from reduced skarns contains lower LREE contents (< 7 ppm) relative to HREE (< 127 ppm; ESM2 Fig. S3). Andradite garnet from oxidized skarn has relatively higher LREE contents (12 to 29 ppm) compared to HREE (0.3 to 10.5 ppm). Light REE contents in clinopyroxene vary from 0.115 to 6.7 ppm and HREE vary from 0.06 to 2.6 ppm (ESM2 Fig. S3).

REE patterns

Scheelite displays five main REE patterns: (i) steep and (ii) shallow negative slope, (iii) concave, (iv) flat to slightly concave, and (v) convex shape (Fig. 9). The steep negative slope pattern is characterized by high $(La/Sm)_{CN}$ and $(Gd/Lu)_{CN}$ ratios (i.e., > 10; Fig. 10), negative to slightly positive Eu anomalies, and is restricted to oxidized skarns scheelite (Fig. 9a). The shallow negative slope pattern has $(La/Sm)_{CN}$ and $(Gd/Lu)_{CN}$ ratios > 1 (Fig. 10), negative and positive Eu anomalies, and occurs in scheelite from both oxidized and reduced skarns (Fig. 9b–c).

The concave pattern is characterized by an enrichment of Pr–Dy relative to La–Ce and Ho–Lu, with $(La/Sm)_{CN}$ < 1 and $(Gd/Lu)_{CN}$ > 10 ratios (Figs. 9d and 10). It occurs mostly in reduced skarn scheelite, with a few samples from oxidized

skarns (i.e., Brejui and Shizhuyuan). The Eu anomaly is predominantly negative, with a few samples displaying positive Eu anomaly (Fig. 9d).

The flat to slightly concave pattern is characterized by $(La/Sm)_{CN}$ < 1 and $(Gd/Lu)_{CN}$ between 1 and 10 (Figs. 9e and 10). It commonly has a negative Eu anomaly and occurs in both reduced and oxidized skarn scheelite; however, reduced skarns have REE scheelite/chondrite ratio > 1, whereas oxidized skarn scheelite has predominantly REE scheelite/chondrite ratio < 1 (Fig. 9e).

The convex pattern, characterized by $(La/Sm)_{CN}$ > 1 and $(Gd/Lu)_{CN}$ < 1 and a positive to slightly negative Eu anomaly, is commonly associated with scheelite from retrograde stages in reduced skarns (Fig. 9d and ESM2 Fig. S4i). One exception is the Jiama oxidized porphyry-skarn Cu deposit, where retrograde scheelite displays a convex pattern (Fig. 9f).

Garnet displays three different REE patterns according to its composition (Figs. 9 and S4). Andradite garnet displays a (i) flat to shallow negative slope pattern with $(La/Sm)_{CN}$ and $(Gd/Lu)_{CN}$ ratios > 1 and positive and negative Eu anomalies (Fig. 9a). In contrast, grossular-spessartite garnet displays a (ii) positive slope with $(La/Sm)_{CN}$ < 1 and $(Gd/Lu)_{CN}$ varying from 0.3 to 2, and (iii) positive slope with flat HREE, which is characterized by $(La/Sm)_{CN}$ < 1 and $(Gd/Lu)_{CN}$ > 2 (Fig. 9b). The Eu anomaly in grossular-spessartite garnet is predominantly positive with few slightly negative values. The Fe-rich clinopyroxene has a flat pattern between La and Ho and a small enrichment from Er to Lu. The Eu anomaly varies from positive to negative (Fig. 9c–d).
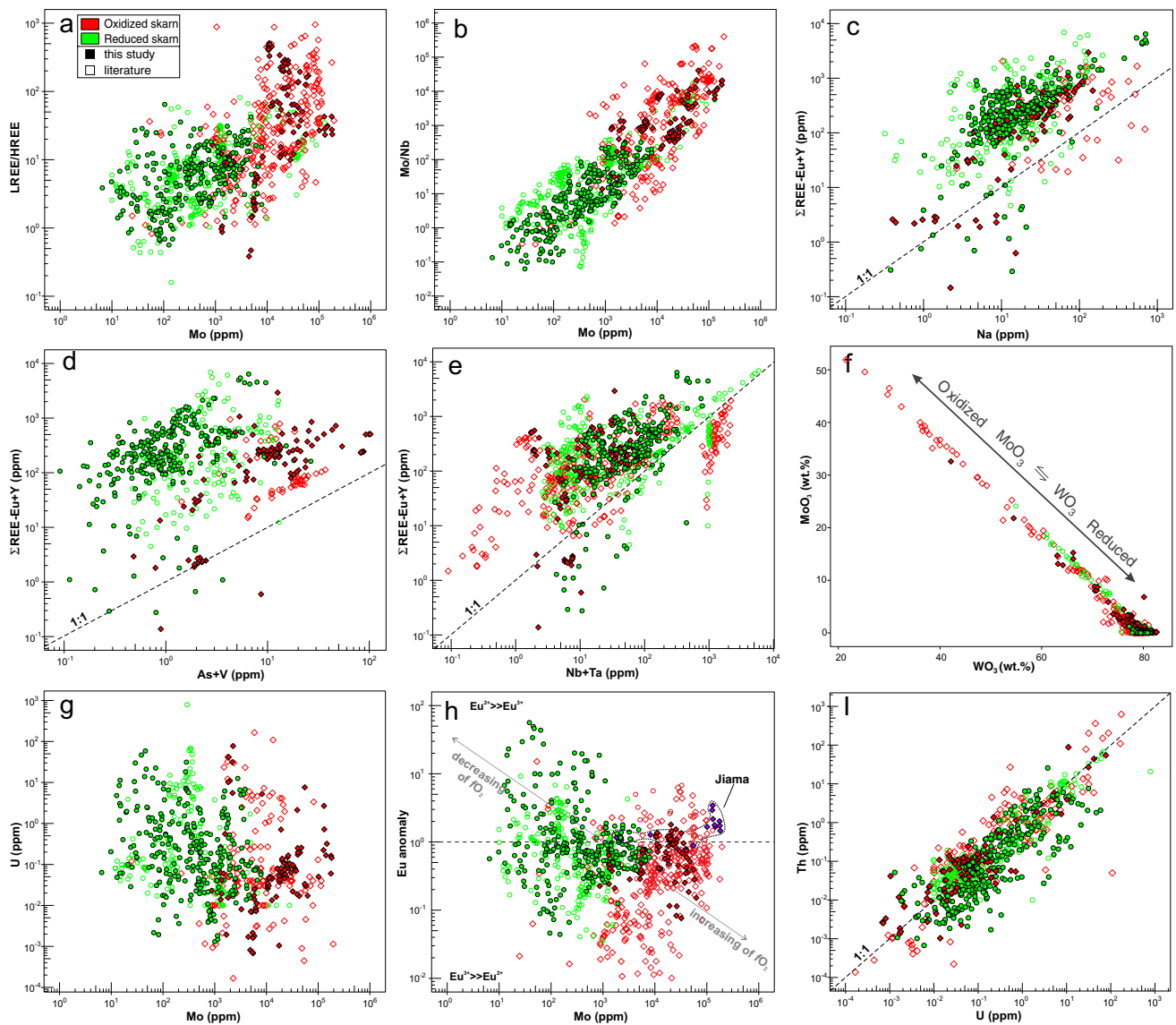
Fig. 6 Binary plots of minor (**f**) and trace (**a–e, g–i**) elements composition scheelite. **a.** Mo versus LREE/HREE, **b.** Mo versus Mo/Nb, **c.** Na versus ΣREE-Eu+Y, **d.** V+As versus ΣREE-Eu+Y, **e.** Nb+Ta versus ΣREE-Eu+Y, **f.** WO$_3$ versus MoO$_3$, **g.** Mo versus U, **h.** Mo versus Eu anomaly, and **i.** U versus Th. Data from: Song et al. (2014), Fu et al. (2016), Guo et al. (2016), Ding et al. (2018), Zhao et al. (2018), Li et al. (2019), Wu et al. (2019), Yuan et al. (2019), Xu et al. (2019), Chen et al. (2020), Seo et al. (2020), Song et al. (2020), and Su et al. (2020)

Figure S4 (ESM2) shows REE patterns of coexisting scheelite, garnet, and clinopyroxene. Scheelite associated with andradite garnet has steep negative slope, whereas garnet displays a flat REE pattern (ESM2 Fig. S4a–c). Positive slope REE pattern scheelite coexists with shallow negative slope pattern grossular-spessartite garnet (ESM2 Fig. S4d–f). Where scheelite and clinopyroxene coexist, scheelite displays both shallow negative slope and concave patterns with a depletion among Er–Lu, whereas pyroxene shows a flat pattern with an enrichment among Er–Lu (ESM2 Fig. S4g–i).

Multivariate statistical analysis of scheelite composition

Scheelite from oxidized and reduced skarns

Figure 11 shows PLS-DA results for LA-ICP-MS scheelite analyses classified according to skarn redox type. The loadings plot (Fig. 11a) of the first and second PLS-DA components (qw*1-qw*2) displays the relationship among variables and groups, whereas the scores plot (Fig. 11b) shows the distribution of the samples in t1–t2 space. In
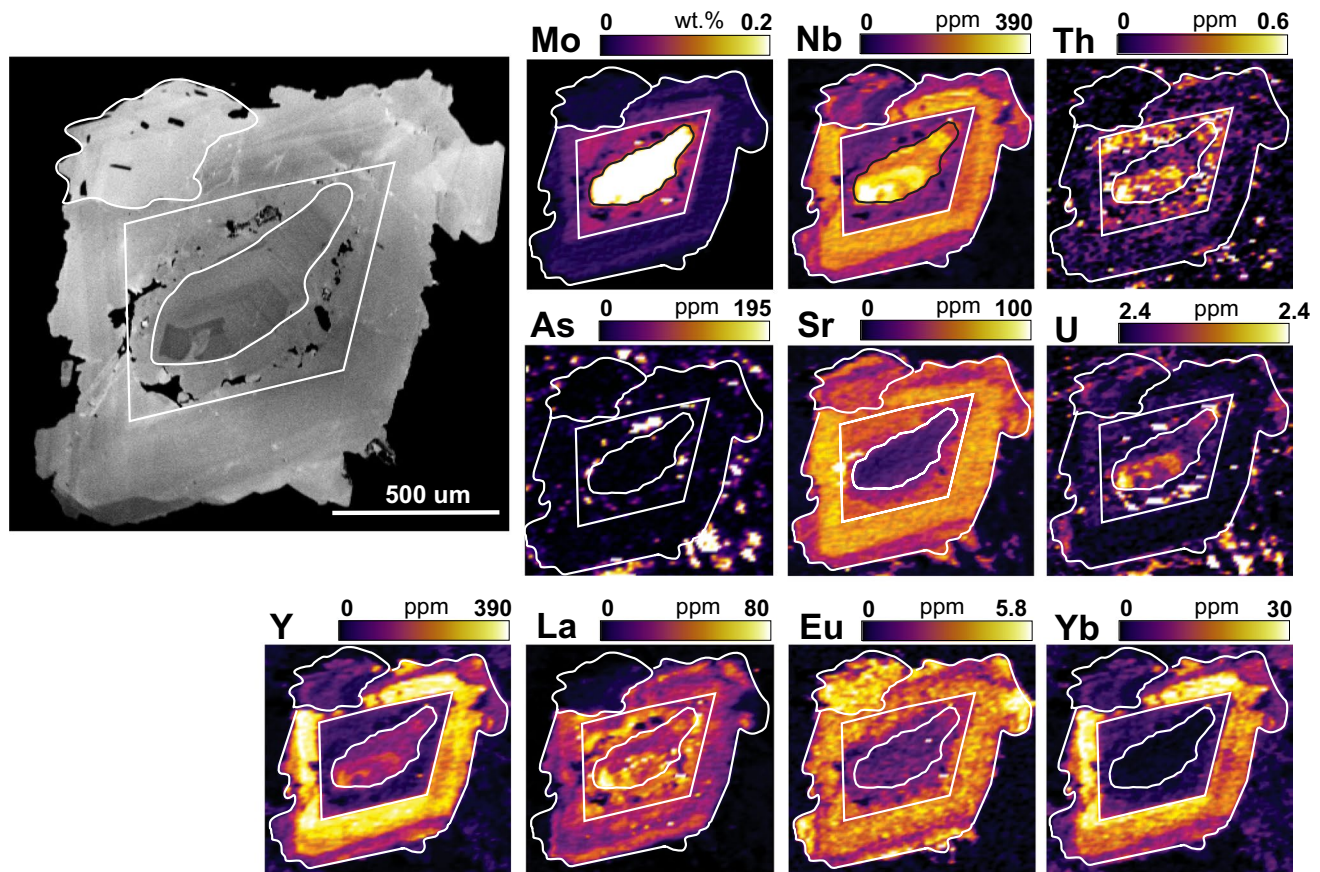
Fig. 7 Cathodoluminescence image (gray scale) and LA-ICP-MS multi-element maps (white-violet scale) showing zoning, dissolution, and overgrown textures in scheelite from amphibole facies, Cantung.

Note the homogenous distribution of As. The concentrations of the elements in the LA-ICP-MS maps are semi-quantitative. The white lines show the grain outline

general, positive correlations exist among Mo, As, and V in negative qw*1 and positive qw*2; Th, U, ΣREE, Ta, and Na in positive qw*1 and qw*2; Nb, Mn and Y, and Ba and Eu anomaly in positive qw*1 and negative qw*2; B, Co, Ni, Ti, and Sr in negative qw*1 and qw*2 (Fig. 11a).

Oxidized skarns plot in the negative qw*1 and positive qw*2, as a result of correlated Mo, As, V, and Ti (Fig. 11a). In contrast, reduced skarns plot at positive qw*1 and negative qw*2 because of correlated Mn, Y, and Nb (Fig. 11a). Therefore, oxidized and reduced skarn classes are mostly discriminated by qw*$_1$ (Fig. 11a). Figure 11b shows that oxidized skarn scheelite plots at negative t1 and spreads in negative and positive t2 due to high Mo, As, V, and Ti concentrations (Fig. 11c). Scheelite from reduced skarns plots mostly at positive t1, and negative and positive t2 because of high Mn, Y, Nb, U, and Eu anomaly contents (Fig. 11b,d). However, few scheelite analyses from reduced skarns plot in negative t1, which overlaps with few samples of oxidized skarn scheelite (Fig. 11b). The elements that best discriminate for redox state skarn classification are Ti, V, Mn, As, Y, Nb, and Mo

(VIP > 1) followed by Co, Th, U, and Eu anomaly (VIP between 0.8 and 1) (Fig. 11e).

Figure 11f displays the same scheelite analyses plotted in the t1–t2 space (Fig. 11b), labeled according to redox state of the granitic intrusions that are associated with the formation of oxidized and reduced skarns. Figure 11f shows a direct relationship between the redox states of skarns and granites, where scheelite associated with magnetite-series granite plots in the oxidized skarn field and scheelite associated with ilmenite(titanite)-series granite plots in the reduced skarn field.

Intrusion composition

Figure 12 displays PLS-DA results of LA-ICP-MS data for scheelite related to the aluminum saturation index of their source felsic intrusions. Figure 12a highlights that peraluminous granites plot at negative qw*1 due to correlated Mn, Mg, and Nb, and at negative qw*2 very close to the qw*2 axis. In contrast, metaluminous granites plot at positive qw*1 because of correlated As and V, and at positive
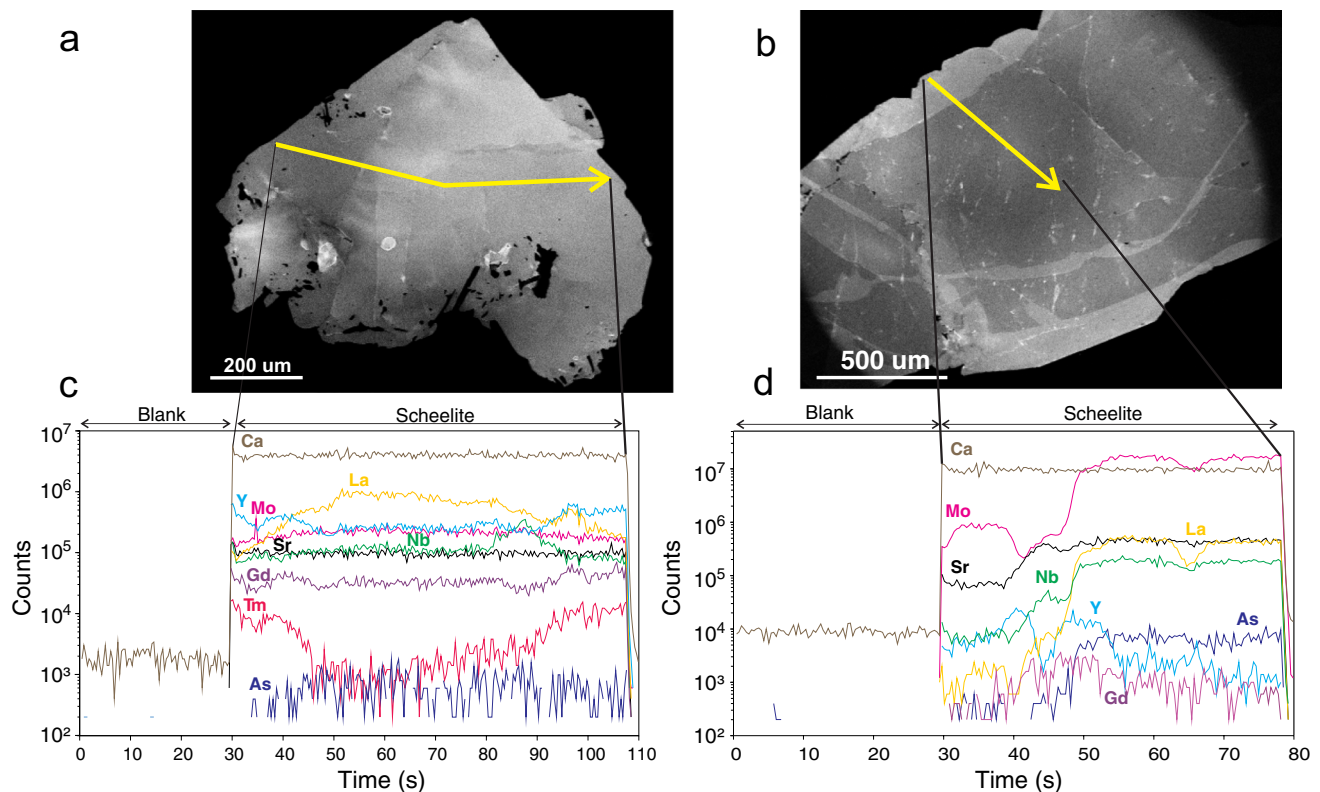
Fig. 8 Cathodoluminescence image showing homogeneous scheelite from Lened in **a**, and homogenous grain overgrown and cut by brighter CL scheelite (Kara) in **b**. The yellow lines indicate the laser-ablation trenches. **c–d.** Time-signal diagram showing the trace element distribution in scheelite along the ablation trenches. Flat patterns indicate homogeneous trace element distribution, whereas irregular profiles indicate heterogeneous element distribution

qw*2 because of correlated U, Th, Y and Pb, and Sr and ΣREE. Therefore, peraluminous and metaluminous granites are mainly discriminated by qw*1 (Fig. 12a).

In the t1–t2 scores plot (Fig. 12b), scheelite related to peraluminous granitic intrusions plots mostly at negative t1 because of high Mn, Mg, and Nb contents and scattered through negative and positive t2. Few analyses plot at negative t1, likely due to higher V and As concentrations relative to the other elements of the peraluminous intrusions (Fig. 12b–c). In contrast, scheelite related to metaluminous granitic intrusions plots mostly at positive t1 and t2, due to high V and As, and U and Th concentrations, respectively (Fig. 12b–d). A few analyses scatter at negative t2, which causes an overlap with analyses of scheelite related to peraluminous granitic intrusions. Figure 12e shows that the most important elements for classification are Mg, V, Mn, As, Nb, Mo, and Ta for VIP > 1, and Ti, Pb, Bi, and U with VIP between 0.8 and 1.

Metal association

Figure 13 displays PLS-DA results of LA-ICP-MS data for scheelite classified in 5 deposit types according to the metal association (Cu-polymetallic, W, W–Au, W–Cu, W–Mo(Sn); Table 1). Figure 13a shows that W–Mo(Sn) and Cu-polymetallic deposits plot at negative qw*1 and positive qw*2 as they correlate with As and Ti, and Co and Ni. The W deposits plot at negative qw*1 and qw*2 because of correlated Mo and V. The W–Au and W–Cu deposits plot at positive qw*1 because of correlated Nb and Mn. The W–Au deposits plot at positive qw*2 due to Na, Th, U, Y and ΣREE correlation and W–Cu deposits plot at negative qw*2 owning to correlated Eu anomaly, Mg, and Ba. Overall, qw*1 discriminates W–Mo(Sn), Cu-polymetallic, and W deposits from W–Cu and W–Au deposits, and qw*2 discriminates W-Mo(Sn), Cu-polymetallic, and W–Au from W and W–Cu deposits.

Figure 13b shows that scheelite associated with W–Mo(Sn) and Cu-polymetallic deposits overlap in negative t1 and positive t2. Scheelite from W–Mo(Sn) and Cu-polymetallic deposits has in common higher contents of Co, Ni, As, and Ti relative to the other deposits. Scheelite from W–Au deposits plots mostly at positive t1 and t2 because of high Y and ΣREE, and low Pb and Sr contents, with few samples plotting at negative t1 and t2, close to the origin. Scheelite from W–Cu deposits shows a wide spread, where
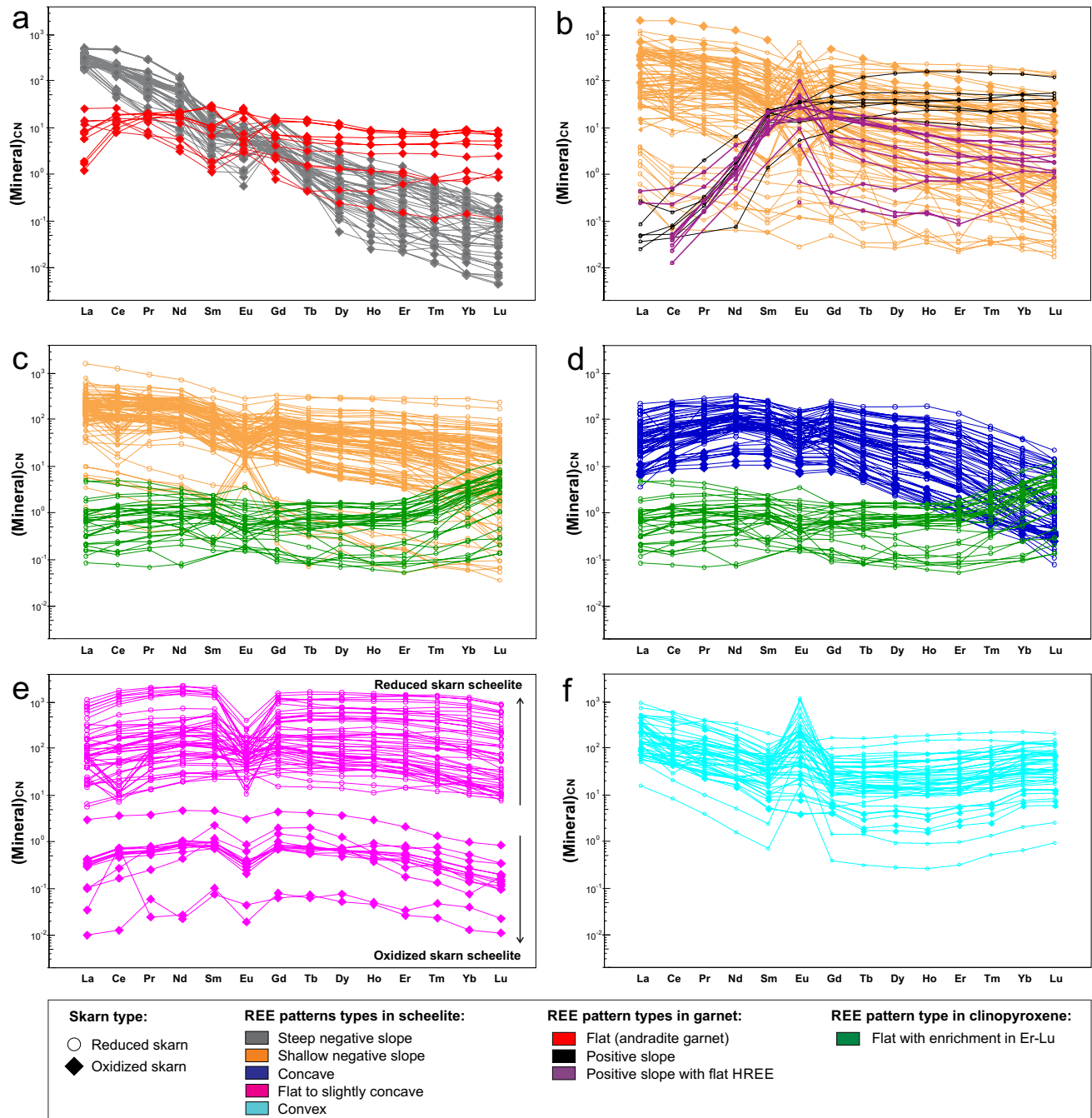
Fig. 9 Chondrite-normalized REE patterns of scheelite, garnet, and clinopyroxene. Chondrite normalized values from McDonough and Sun (1995). **a.** Steep negative slope in scheelite coexisting with flat pattern in garnet. **b.** Shallow negative slope in scheelite coexisting with positive slope pattern in garnet. **c.** Shallow negative slope with a slight depletion between Er–Lu pattern in scheelite coexisting with flat pattern with a slight enrichment among Er–Lu in clinopyroxene. **d.** Concave shape with a depletion among Er–Lu coexisting with flat pattern with a slight enrichment among Ho–Lu in clinopyroxene. **e.** Flat to slightly concave shapes with scheelite/chondrite ratio > 1 for reduced skarns and < 1 for oxidized skarns. **f.** Convex shape

most analyses plot at positive t1 and negative t2 due to higher Nb and Mn concentrations, and with few scheelite analyses with positive t1 and t2. Few scheelite analyses from W–Cu deposits plot at negative t1 and t2 overlapping with scheelite from W deposits (Fig. 13a–b). Scheelite from W

deposits plots mostly at negative t1 and t2, because of higher Mo and Pb concentrations relative to the origin. A small group of few scheelite analyses plot at negative t1 and positive t2 due to their higher Co and Y concentrations relative to the others scheelite from W deposits.

Fig. 10 Binary plot (Gd/Lu)$_{CN}$ versus (La/Sm)$_{CN}$ showing the relation between these ratios and the REE patterns on scheelite
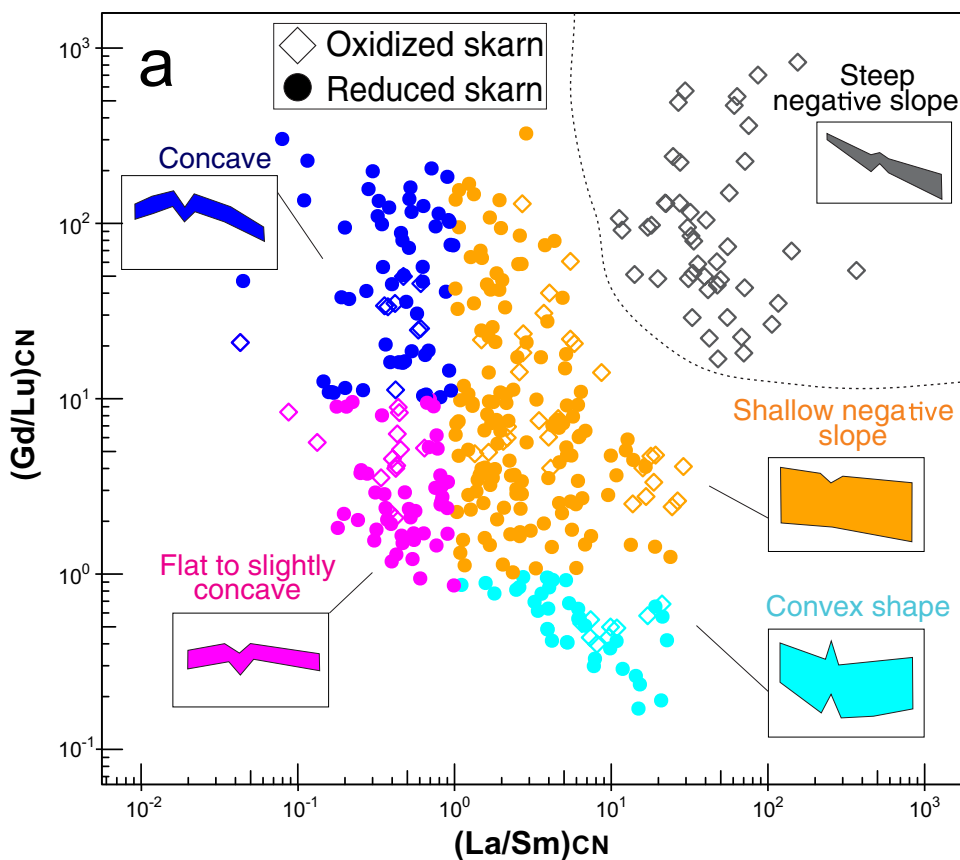

Discussion

Scheelite trace element substitution

Scheelite has a tetragonal structure with two cation sites: a dodecahedral coordination occupied by $[CaO_8]^{14-}$ groups and a tetrahedral coordination occupied by $[WO_4]^{2-}$ groups. Elements with similar electron configuration and ionic radii to Ca (i.e., Sr, Pb, Mn, Y, ΣREE) and W (i.e., Mo, V, As, Nb, Ta) commonly substitute into the scheelite lattice (Ghaderi et al. 1999; Poulin et al. 2018; Sciuba et al. 2020).

The $ΣREE^{3+}$ and Y^{3+} are incorporated as follow (Nassau 1963; Burt 1989; Ghaderi et al. 1999):

$$2Ca^{2+} = (REE, Y)^{3+} + (Na)^{+} \qquad (1)$$

$$Ca^{2+} + W^{6+} = +(REE, Y)^{3+} + (V, As, Nb, Ta)^{5+} \qquad (2)$$

Figure 13c displays the first and third components (qw*1–qw*3), where W–Mo(Sn) deposits are better discriminated from Cu-polymetallic deposits relative to qw*1–qw*2 plot (Fig. 13a). Scheelite from Cu-polymetallic and W deposits plot at negative qw*1 and qw*3 as they correlated to V and Mo. The W–Mo(Sn) deposits plot at negative qw*1 because of Ti, As, and Mo correlation, but qw*3 is not discriminant. Tungsten-Au and W–Cu deposits plot close to each other at positive qw*1 and qw*3 owing to correlated Ta, Eu anomaly, ΣREE, Mg, and Na.
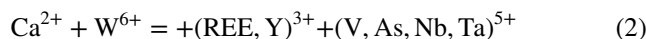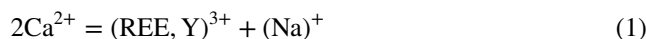
Figure 13d shows significant overlaps between: (i) scheelite from W–Cu and W–Au deposits that spread from positive t1 and negative t2 toward negative t1 and positive t2, and have in common high Nb, Mn, and Y concentrations and; (ii) scheelite from W–Mo(Sn) and W deposits that plot at negative side of t1, but through positive and negative t2. Scheelite Cu-polymetallic deposits plots separately from the others scheelite at negative t1 and t3, due to high V and Mo concentration (Fig. 13d).
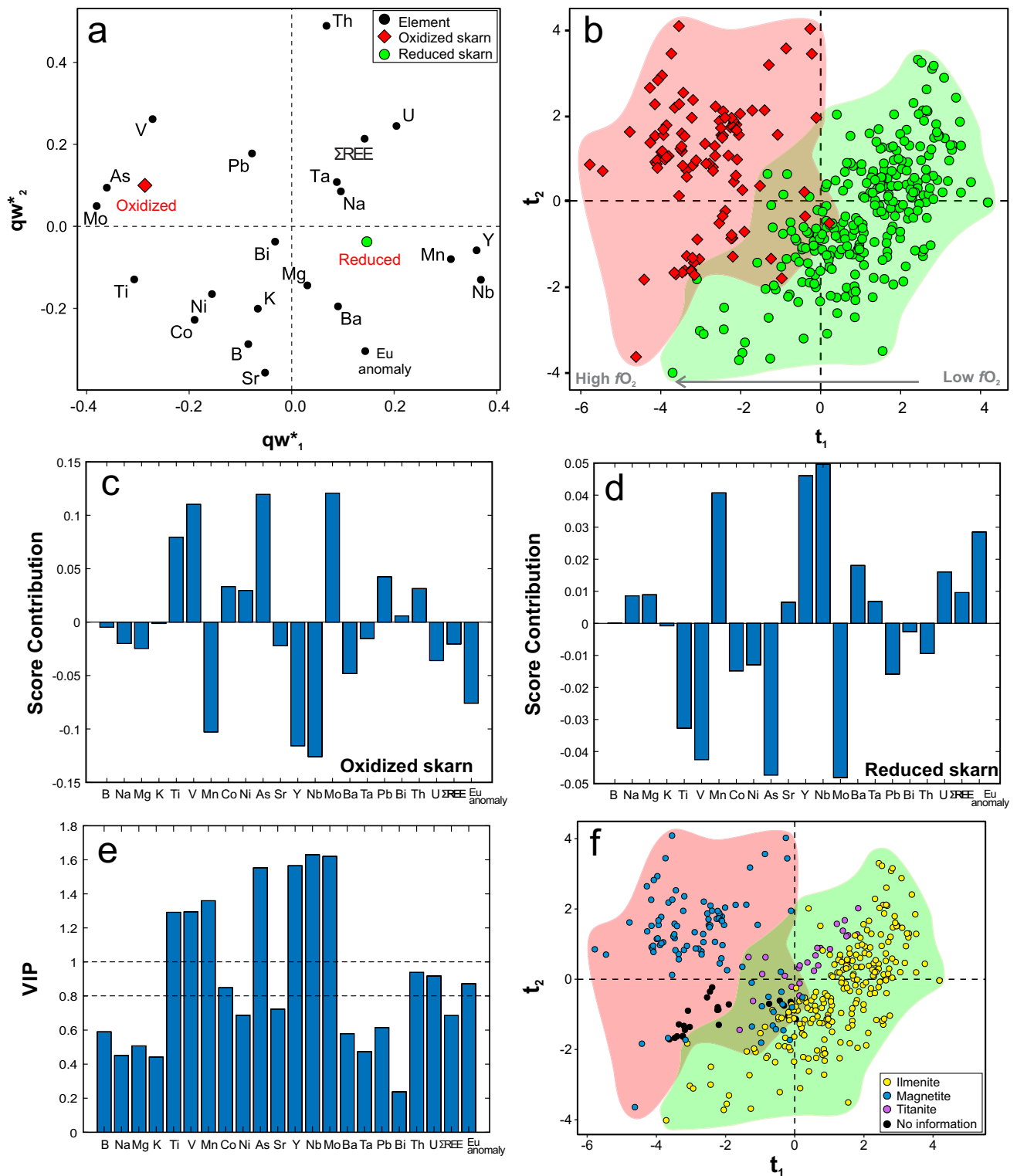
Fig. 11 Partial least squares discriminant analysis (PLS-DA) of LA-ICP-MS data for scheelite from skarn systems. **a.** qw*1–qw*2 (first and second loadings) plot showing the correlations among elemental variables and skarn types (oxidized vs reduced). **b.** t1–t2 (first and second scores) plot showing the distribution of scheelite analyses in the latent variable space defined by qw*1–qw*2. **c–d** Score contributions of scheelite associated with oxidized (**c**) and reduced (**d**) skarns

indicating the main elements that contribute to classification. **e.** Variable Importance on Projection (VIP) plot showing the importance of compositional variables in classification of the model in (**b**). **f.** Projection of the compositional data of scheelite analyses labeled by the oxidation state of the intrusion related to skarn mineralization in the t1–t2 plot (**b**)

$$3Ca^{2+} = 2REEY^{3+} + Ca_{vac}, where Ca_{vac} is a vacancy site \quad (3)$$
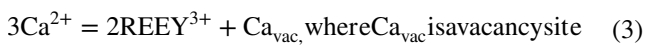
For substitution, (i) the sum of monovalent cations must be equal to all trivalent REE and Y, since 1+cations provide the charge balance in scheelite structure. The MREE (Sm-Dy) are preferentially incorporated in the dodecahedral site relative to LREE (La–Nd) and HREE (Ho–Lu), which characterizes the bell-shaped/MREE-enriched pattern as exemplified by Ghaderi et al. (1999) in scheelite from Archaean gold deposits in Western Australia. For equation, (ii) the sum of Nb, Ta, As, and V also needs to be similar to that of REE and Y (Dostal et al. 2009).

Among the monovalent cations hosted in scheelite (K and Na), only Na is positively correlated with trivalent REE and Y (Fig. 6c and ESM2 Fig. S1a). Niobium, Ta, As, and V also display a positive correlation with REE and Y (Fig. 6d–e), suggesting that REE and Y are, at least in part, incorporated through mechanism (ii). However, the sum of Na, Nb, Ta, As, and V is lower than the sum of REE and Y (ESM2 Fig. S1b), which suggests that part of the REE and Y are incorporated by substitution (iii). In this case, as substitution (iii) does not depend on a coupled substitution to maintain crystal neutrality, the scheelite REE signature is directly controlled by that of the fluid (Ghaderi et al. 1999; Song et al. 2014).

Strontium^{2+} and Pb^{2+} are readily incorporated into Ca^{2+} site as they have similar ionic radii and valence state (Dostal et al. 2009; Sciuba et al. 2020). The Mn^{2+} and Mg^{2+} incorporation is limited because they have smaller cations relative to Ca^{2+} ($^{[VIII]}$Mn^{2+}: 0.96; $^{[VIII]}$Mg^{2+}: 1.03; $^{[VIII]}$Ca^{2+}: 1.12) and prefer monoclinic structure (Ghaderi et al. 1999; Dostal et al. 2009). This may explain their lower contents in scheelite (Fig. 5). Although Mn occurs in low content, it is an important element (VIP > 1) for discrimination of reduced and oxidized skarn scheelite (Fig. 11). Manganese is widely accepted to be transported as MnCl$_2$ or MnCl$^-$ complexes in crustal fluids (Tian et al 2014; Brugger et al. 2016). Stokes et al. (2019) and Bromiley et al. (2021) showed that the magma fO_2 does not affect the concentration of Mn in magmatic apatite, which is commonly found as Mn^{2+} form. Given that Mn occurs as MnCl$_2$ or MnCl$^-$ complexes in crustal fluids (Tian et al. 2014; Brugger et al. 2016) and assuming that magma fO_2 does not affect the Mn redox state, a possible explanation for the higher Mn concentration in reduced skarns relative to oxidized skarn could be magma composition because the majority of reduced skarns are related to peraluminous felsic intrusions that have high Mn concentration (Table 1; Fig. 12).

Scheelite forms a solid solution with powellite (CaMoO$_4$) through the simple substitution of W^{6+} for Mo^{6+} (Fig. 6f). This substitution is strongly favored by high fO_2 in the hydrothermal system, where Mo migrates as Mo^{6+} and thus substitutes for W^{6+} in scheelite (Hsu 1977). Scheelite associated with high fO_2 systems has higher Mo content than that associated with low fO_2 systems (Figs. 5, 6f, and 11) as confirmed by our dataset and Xu et al. (2020).

Molybdenum is the main element that causes different textural zonings in scheelite reveled by CL imaging (Figs. 4, 7–8; ESM2 Fig. S2), and Nb, Th, and U are often concentrated in few zones through the scheelite crystal (Fig. 7; ESM2 Fig. S2). Oscillatory zoned scheelite grains commonly occur during the prograde stage, and less commonly during the retrograde stage (Fig. 4). As Mo incorporation in scheelite is mainly controlled by the fO_2 of hydrothermal fluids (Hsu 1977), the oscillatory zoning (ESM2 Fig. S2; Fig. 7) is likely due to fluctuations of the redox conditions. Scheelite crystallized from retrograde fluids is predominantly homogeneous, which suggest more constant hydrothermal fluid fO_2. Retrograde stage scheelite has relatively lower Mo content relative to prograde stage (Figs. 7–8) due to Mo depletion as a result of earlier deposition of scheelite (Einaudi et al. 1981; Choi et al. 2020; Su et al. 2020).

Arsenic, V, Nb and Ta are incorporated in the scheelite lattice according to (ii) substitution mechanism (Nassau 1963; Burt 1989; Brugger et al. 1998; Ghaderi et al. 1999), as shown by their broad correlation with ΣREE (Fig. 6d–e). Similar to Mo, As and V incorporation in scheelite is dominantly controlled by the redox conditions. At high fO_2, As^{5+} and V^{5+} form H$_3$AsO$_{4(aq)}$ and H$_3$VO$_{4(aq)}$ complexes (Testemale et al. 2004; James-Smith et al. 2010; Brugger et al. 2016) which have similar ionic radii to W ($^{[IV]}$W^{6+}: 0.42 Å; $^{[IV]}$As^{5+}: 0.335 Å; $^{[IV]}$V^{5+}: 0.355 Å; Shannon 1976). At lower fO_2, As and V (less soluble) are transported in more reduced forms $^{[VI]}$As^{3+} (0.58 Å) and V ($^{[VI]}$V^{4+}: 0.58 Å; $^{[VI]}$V^{3+}: 0.64 Å; Shannon 1976) as As(OH)$_{3(aq)}$ and VO^{2+}/VOH^{2+} complexes (Testemale et al. 2004; James-Smith et al. 2010; Brugger et al. 2016), which are less compatible to enter scheelite structure. This may explain their lower concentration in scheelite from reduced skarns (Figs. 5 and 11).

Unlike As and V, the Nb concentrations are higher in scheelite from reduced relative to oxidized skarns (Figs. 5 and 11). Higher Nb contents coincide with lower Mo concentrations (ESM2 Fig. S2; Fig. 7). According to Zhao et al. (2018), the presence of Mo in hydrothermal fluid has a negative effect on Nb incorporation into the scheelite structure as $^{[IV]}$Nb^{5+} (0.48 Å) and $^{[IV]}$Mo^{6+} (0.41 Å) occupy the same $^{[IV]}$W^{6+} (0.42 Å; Shannon 1976) site and scheelite-powellite solid solution results from the preferential incorporation of Mo^{6+} into scheelite at high fO_2. At moderate to low fO_2 conditions, Mo is dissolved in the hydrothermal fluid as both $^{[IV]}$Mo^{5+} (0.46 Å) and $^{[VI]}$Mo^{4+} (0.65 Å) states (Hsu 1977; Zhao et al. 2018), which form the coupled substitution:

(i) $\quad Ca^{2+} + Mo^{6+} = \sum REE^{3+} + (1-x)Mo^{5+} + xNb^{5+} (0 \leq x \leq 1)$ (Zhao et al. 2018).
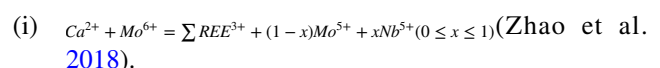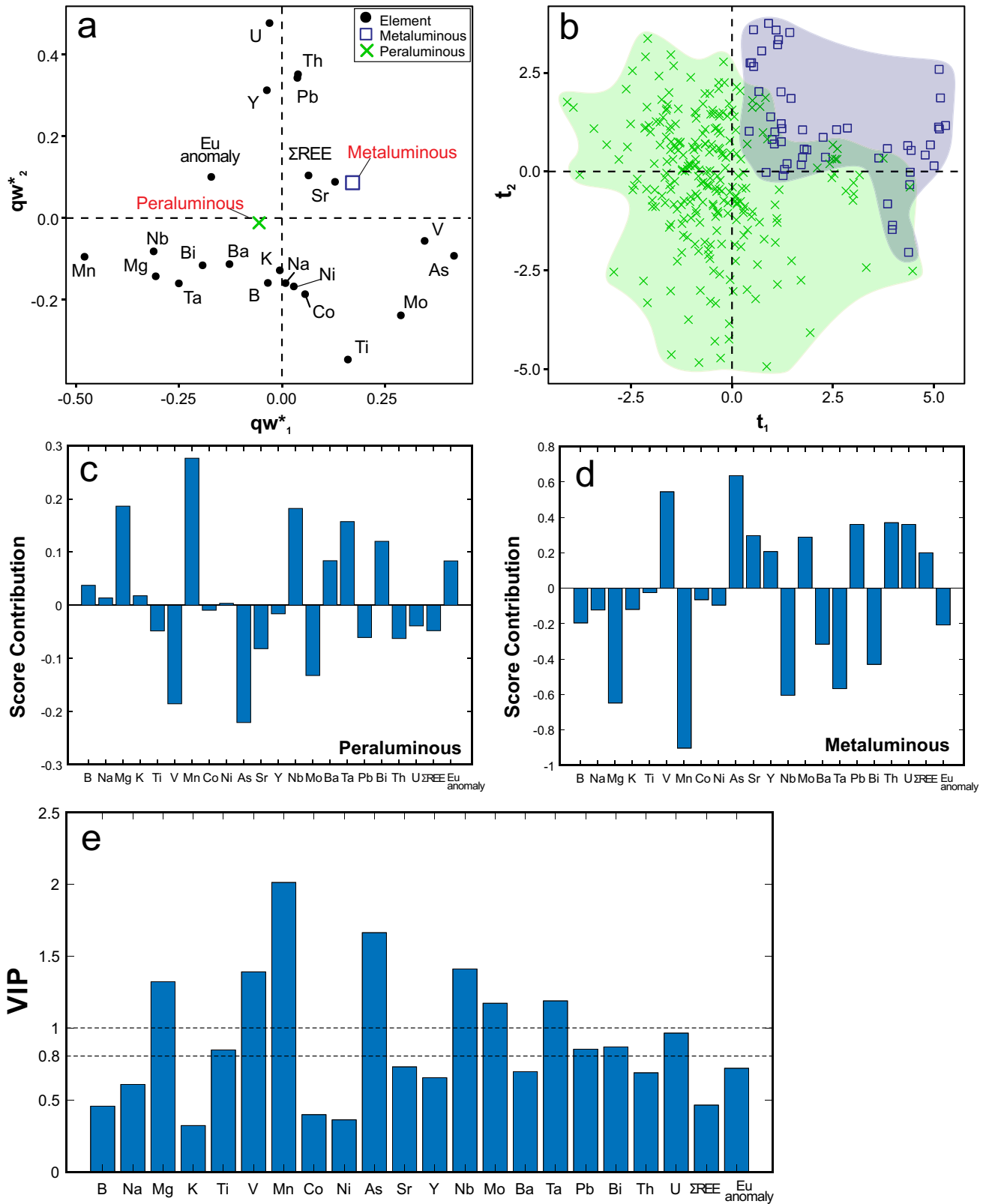
High $Mo^{6+}/(Mo^{5+} + Mo^{4+})$ ratios in hydrothermal fluids inhibit Nb incorporation into scheelite, whereas lower $Mo^{6+}/(Mo^{5+} + Mo^{4+})$ ratios favor it. Such correlation is supported by low Mo/Nb ratios in scheelite from reduced skarns (0.06 to 324) relative to higher Mo/Nb ratios in oxidized skarns (from 5 to 40,577; Fig. 6b).

◄**Fig. 12** Partial least squares discriminant analysis (PLS-DA) of LA-ICP-MS data for scheelite from skarn systems. **a.** qw*1–qw*2 (first and second loadings) plot showing the correlations among elemental variables and intrusion composition (peraluminous and metaluminous). **b.** t1–t2 (first and second scores) plot showing the distribution of scheelite analyses in the latent variable space defined by qw*1–qw*2. **c–d.** Score contributions of scheelite associated with peraluminous (**c**) and metaluminous (**d**) intrusions indicating that each group is discriminated by distinct mean composition, and the main elements that contribute for each group. **f.** VIP plot showing the importance of compositional variables in classification of the model in **b**

Higher U and Th concentrations coincide with darker zones in CL images in both skarn types (ESM2 Fig. S2; Fig. 7). Su et al. (2019) showed similar features with CL images of scheelite from the Dabaoshan porphyry Mo–W deposit, suggesting that U replaces W in scheelite, since U^{6+} has similar ionic configurations to W^{6+}, and displays a negative correlation with Mo. Thorium is incorporated into the Ca site because Th has a similar ionic radii ($^{[VIII]}Th^{4+}$: 1.05 Å and $^{[VIII]}Ca^{2+}$: 1.12 Å; Shannon 1976; Sun et al. 2019). Uranium and Mo show weak negative correlations in reduced skarns and display no correlation in oxidized skarn scheelite (Fig. 6h). Such weak correlations suggest that U may not necessarily substitute for W but instead for Ca. Given that U also exists as U^{4+} ($^{[VIII]}U^{4+}$: 1 Å) and is positively correlated to Th (Fig. 6i), we suggest that both U and Th may be incorporated together as follows:

$$2Ca^{2+} = (U, Th)^{4+} + Ca_{vac}, where\ Ca_{vac}\ is\ a\ vacancy\ site$$
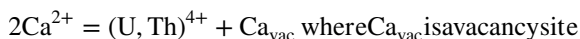
This substitution may explain the low concentration of both U and Th in skarn scheelite (Fig. 5), given the valence state differences between $(U,Th)^{+4}$ and Ca^{2+}. However, more work is required to better understand U and Th incorporation in scheelite.

Titanium concentration is higher in oxidized relative to reduced skarn scheelite (Fig. 5), yet its distribution is not affected by fO_2. In hydrothermal fluids, Ti is commonly transported as Ti^{4+}, and its solubility increases with increasing fluid salinity, temperature, and pressure (Ayers and Watson 1993; Purtov & KoteVnikova 1993; Ryzhenko et al. 2006). Given that oxidized skarns are formed from higher salinity fluids relative to reduced skarns (Table 1), and Ti^{4+} can be incorporated into either W or Ca sites ($^{[IV]}Ti^{4+}$: 0.42 Å versus $^{[IV]}W^{+6}$: 0.42 Å, and $^{[VIII]}Ti^{4+}$: 0.74 Å versus $^{[VIII]}Ca^{2+}$: 1.12 Å; Shannon 1976), the salinity is likely a contributing factor for the higher Ti concentrations in oxidized skarn scheelite (Figs. 5 and 11).

REE patterns

Negative slope REE patterns are the most common in scheelite from skarn systems (Song et al. 2014; Guo et al. 2016). Li et al. (2019) observed that less fractionated REE patterns (slightly concave to flat) are commonly associated with retrograde stage scheelite. This study confirms these findings but also shows that the negative slope REE pattern can be divided in two types, steep and shallow negative slope REE patterns, with distinct (La/Sm)CN and (Gd/Lu)CN ratios (Fig. 10), with the steep negative slope REE pattern being restricted to oxidized skarn scheelite (Figs. 9a and 10).

Song et al. (2014) suggested that the steep negative slope REE pattern in scheelite from oxidized skarns at Chizhou (China) is caused by co-precipitation of andradite garnet. In this case, garnet incorporates preferentially HREE over LREE causing HREE depletion in hydrothermal fluids (Song et al. 2014). Our results show that Fe-rich garnet, associated with steep negative slope REE pattern, has a flat REE pattern with no enrichment in HREE relative to LREE (Fig. 9a), which is a typical REE pattern for andradite garnet (Gaspar et al. 2008; Ismail et al. 2014; Xu et al. 2020). For this sample suite, garnet crystallization cannot explain the REE fractionation in scheelite.

Factors such as fluid composition, redox, and salinity can lead to the fractionation of REE during transport (Haas et al. 1995; Migdisov et al. 2016). In high salinity fluids, LREE are more stable as chloride complexes relative to HREE (Migdisov et al. 2016). Given that prograde oxidized skarn scheelite formed from fluids with higher salinities than those of reduced skarns (up to 60 wt.% NaCl equiv. versus up to 14 wt.% NaCl equiv. for reduced skarns; Table 1), such differences of salinity would explain the stronger REE fractionation in oxidized skarn prograde scheelite.

In reduced skarns, the typical grossular-spessartite garnet displays a strong HREE enrichment relative to LREE (Fig. 9b), and clinopyroxene has a flat REE pattern from La to Dy, with a slight enrichment from Ho to Lu (Fig. 9c–d). In cases where scheelite co-crystalized with garnet (Fig. 9b; ESM2 Fig. S4d–f), scheelite displays a shallow negative slope REE pattern and in cases where it co-crystalizes with clinopyroxene (Fig. 9c–d; ESM2 Fig. S4d–f), the scheelite REE pattern is depleted in Er to Lu. Unlike in oxidized skarn, we suggest that the co-crystallization of grossular-spessartite garnet and clinopyroxene in reduced skarns fractionate HREE in the fluids, yielding scheelite REE patterns slightly depleted from Ho–Lu relative to La-Dy (Fig. 9b–d; ESM2 Fig. S4d–i).

Brugger et al. (2000) showed that scheelite from Mt. Charlotte orogenic gold deposit (Australia) has concave and convex REE patterns, where the convex REE pattern is the result of fractional crystallization of scheelite in a closed system. Because the partition coefficients for MREE (Sm-Dy) between scheelite and the fluid are relatively higher than for LREE and HREE (Brugger et al. 2000), the early scheelite to crystalize has a concave REE pattern, causing depletion of MREE in the fluid resulting
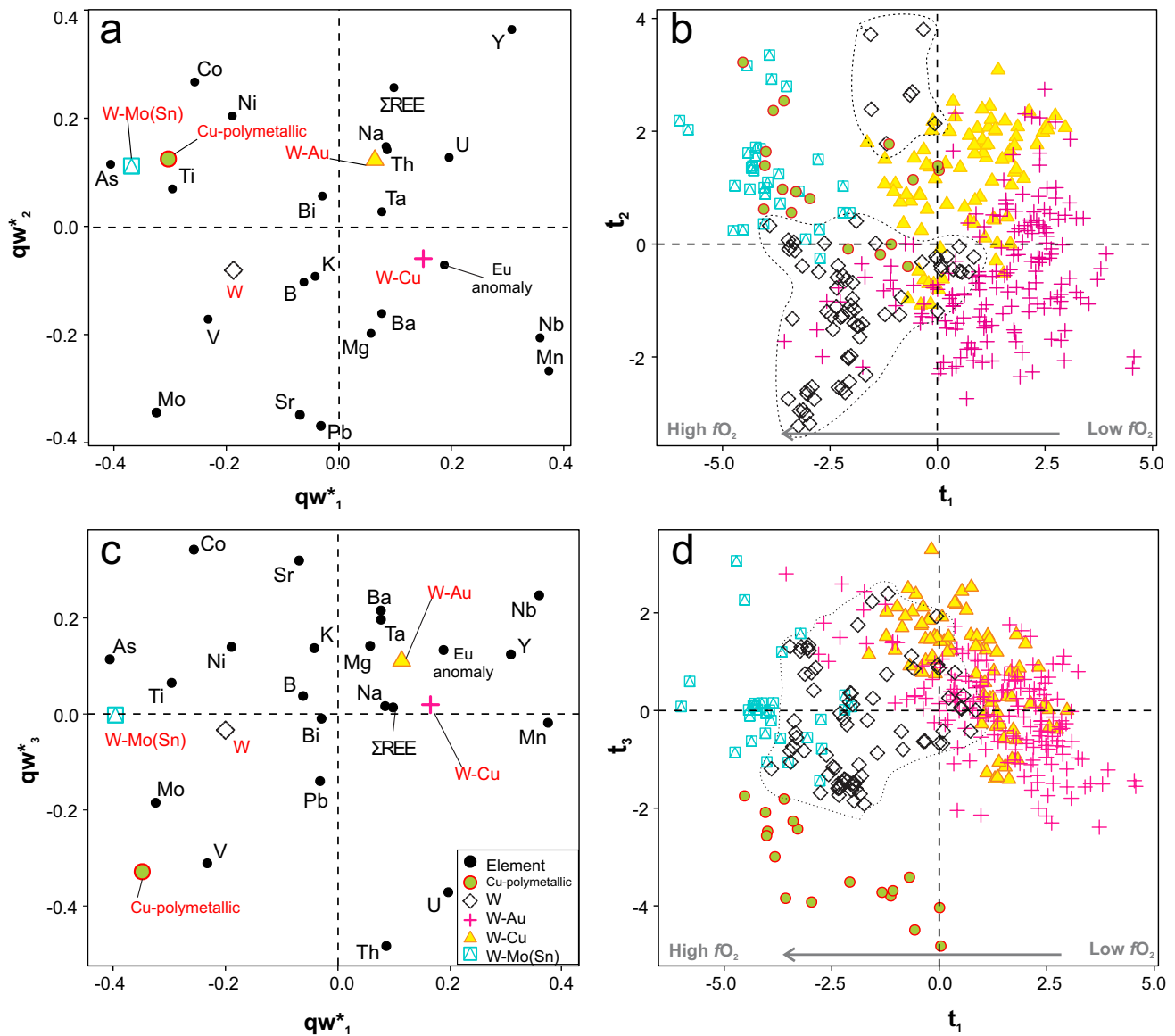
Fig. 13 Partial least squares discriminant analysis (PLS-DA) of LA-ICP-MS data for scheelite from skarn systems. **a.** qw*1–qw*2 (first and second loadings) plot showing correlations among elemental variables and metal associations. **b.** t1–t2 (first and second scores) plot showing the distribution of scheelite analyses in the latent variable space defined by qw*1–qw*2. **c.** qw*1–qw*3 (first and third loadings) plot showing the correlations among elemental variables and metal association. **d.** t1–t3 (first and third scores) plot showing distribution of scheelite analyses in the latent variable space defined by qw*1–qw*3

in the latest scheelite with a convex REE pattern. Zhang et al. (2018) reported similar findings for scheelite from the vein and disseminated Shimensi W deposit in South China. Given that the convex REE pattern is restricted to scheelite crystallized during the late stages of skarn systems, this pattern probably results from MREE incorporation in early scheelite (ESM2 Figs. S4 and S5).

Eu anomaly

The Eu anomaly is commonly used as a qualitative indicator to track the redox conditions of fluids or melts (Sverjensky 1984; Zhang et al. 1990). A positive Eu anomaly indicates an abundance of Eu^{2+} relative to Eu^{3+} in the fluids, suggesting more reduced conditions, and a negative Eu anomaly

indicates abundance of Eu^{3+}, and more oxidized conditions. In the case of scheelite, caution is in order in interpreting redox conditions as Eu is incorporated into the Ca site of scheelite; regardless of its oxidation state, Eu^{2+} is more readily incorporated over Eu^{3+} because of its valence and ionic radii similarity to Ca^{2+} (Ghaderi et al. 1999; Brugger et al. 2000, 2008).

Scheelite from reduced and oxidized skarns system displays both positive and negative Eu anomalies (Fig. 6h). Strong negative Eu anomalies are limited to oxidized skarn scheelite, and strong positive Eu anomalies are limited to reduced skarns, which matches with the redox state of each system (Fig. 6h). A broad negative correlation between the Eu anomaly and Mo content suggests that the Eu^{2+}/Eu^{3+} ratio of scheelite increases with decreasing fO_2 (Fig. 6h), given that low Mo content is an indicative of low fO_2 (Hsu 1977). The Eu anomaly in scheelite does not seem to be totally controlled by the fO_2, given that negative Eu anomalies are also observed in reduced skarn scheelite. A plausible explanation could be that the Eu anomaly is inherited from the mineralizing fluid extracted from the residual melt of felsic intrusions, which commonly have a negative Eu anomaly due to crystallization of feldspar (Drake and Weill 1975; Baker et al. 2004).

In oxidized skarn scheelite, positive Eu anomalies (from 2 to 3.4) are associated with the highest Mo concentrations (Jiama porphyry-skarn Cu deposit, 12 to 17 wt.% of Mo; Fig. 6h). The felsic intrusion related to mineralization at Jiama displays weak negative Eu anomalies (Zheng et al. 2016), so the positive Eu anomalies in Jiama scheelite cannot be explained by high Eu content of mineralizing fluid sourced from this intrusion. Salinity and the nature of the REE ligands can cause changes in the Eu anomaly (Migdisov et al. 2016), since the Eu^{2+} cation is more stable in Cl-rich fluids whereas Eu^{3+} is more easily mobilized by OH complexes (Sverjensky 1984; Bau 1991; Haas et al. 1995). The Jiama porphyry-skarn Cu deposit is dominated by Cl-rich saline fluids (< 36 wt.% NaCl eq.; Zheng et al. 2016), so Eu^{2+} would be preferentially transported as chloride complexes relative to Eu^{3+}, yielding positive Eu anomalies in scheelite. The positive Eu anomalies can also be related to local variation of the pH of mineralizing fluids due to fluid-rock interaction (Brugger et al. 2008).

Use of scheelite chemistry as discriminant of skarn type, source of mineralizing fluids, and deposit types

Skarn type and source of the mineralizing fluid

The PLS-DA results show that scheelite composition varies following skarn redox state, intrusion composition, and metal association (Figs. 11–13). Scheelite from oxidized skarns, metaluminous felsic intrusions, and from Cu-polymetallic, W–Mo(Sn), and W deposits have in common high concentrations of Mo, As, and V. Scheelite from reduced skarns, peralunimous felsic intrusions, and W–Au and W–Cu deposits have in common low Mo, As, and V, and high Mn, Nb, and Ta concentrations (Figs. 11–13). These results suggest that scheelite chemistry is strongly dependent on composition of mineralizing fluids, which are partially controlled by the chemical composition of the felsic intrusion, so the chemical variations of scheelite can be used to discriminate skarn redox state, fluids source, and deposit types.

The redox state of skarns depends either on the redox potential of the host rocks or the fO_2 of the source magma (Einaudi et al. 1981; Newberry and Swanson 1986; Chang et al. 2019). The redox potential of the different rocks hosting the investigated scheelite skarn deposits is difficult to estimate. The majority are hosted in limestone and/or carbonaceous-rich (reduced) rocks having a relatively similar redox potential. The fO_2 of magmas controls skarn redox state as reduced skarns are dominantly associated with ilmenite- and titanite-bearing intrusions, and oxidized skarn with magnetite-bearing intrusions (Table 1). The control of magmas fO_2 on scheelite composition is supported by the concentration of elements sensitive to the oxidation state of the fluid (e.g., Mo, As, V) that correlates with the oxidation state of magma (Fig. 11f).

The metal association is largely controlled by the redox state and fractionation degree of the magma in magmatic-hydrothermal systems (Chang et al. 2019). Intrusion-related Cu–Mo deposits are commonly associated with more oxidized magmas and Sn, and some Au deposits are commonly related to more reduced magmas (Ishihara 1977; Belvin and Chappell 1992; Thompson et al. 1999). Tungsten deposits can be related to both redox type magmas. Because scheelite records both fO_2 and the chemical affinity of granitic magma (Figs. 11a–b and 12a–b), our results show that scheelite can be used to discriminate different metal association in intrusion-related deposits (Figs. 13a–d).

Scheelite from different deposit types

Several discrimination diagrams based on Mo, Sr, and REE concentrations in scheelite have been proposed (Song et al. 2014; Poulin et al. 2018; Sciuba et al. 2020). Song et al. (2014) suggested that the differences in LREE (La–Nd), MREE (Sm–Dy), and HREE (Ho–Lu) concentrations in scheelite may be used to separate skarn-porphyry and Au–W quartz vein deposits. Poulin et al. (2018) and Sciuba et al. (2020) showed that the Sr/Mo ratio versus Eu anomaly discriminate scheelite from metamorphic environments from those from magmatic-hydrothermal settings, although there
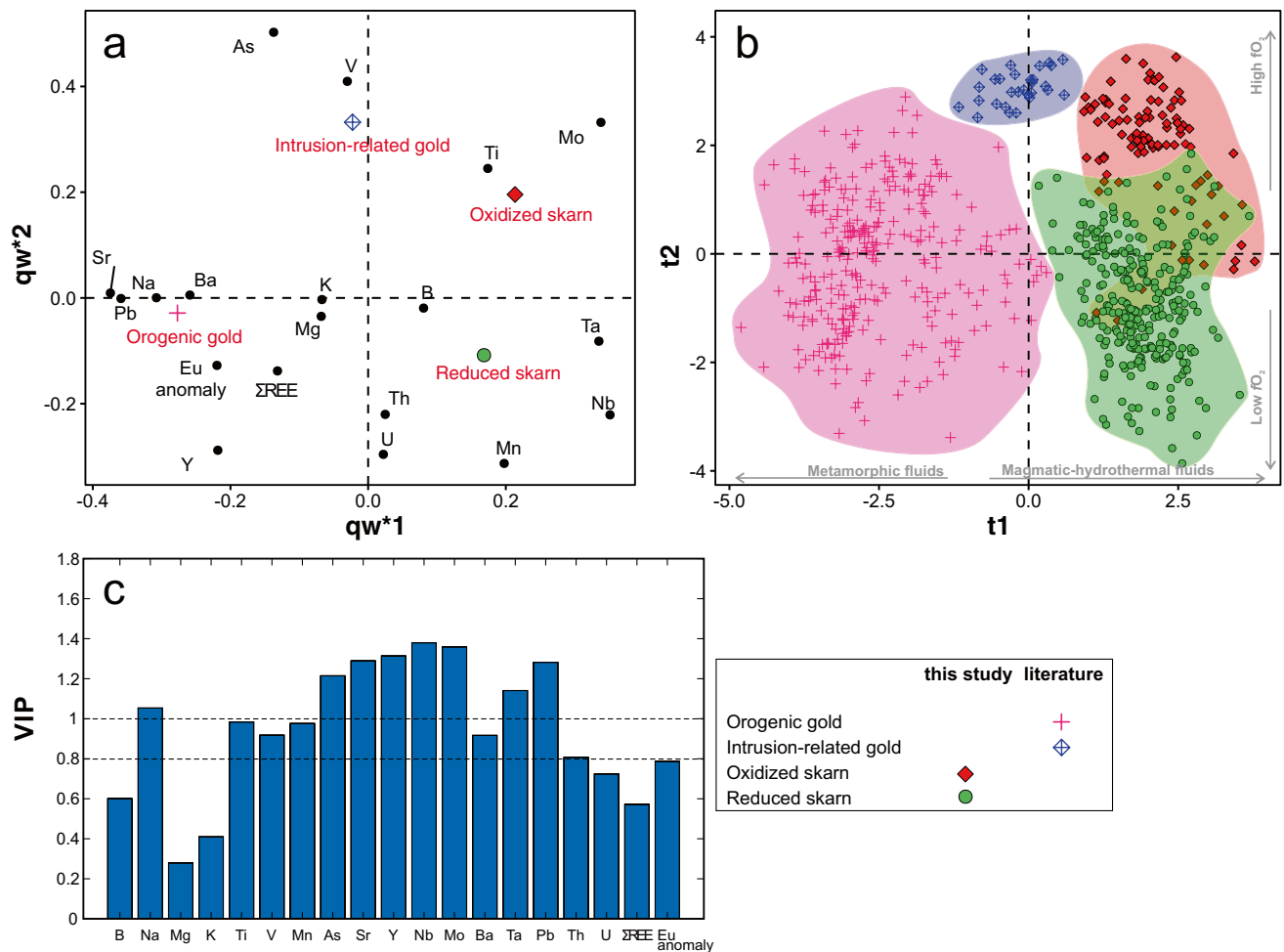
Fig. 14 Partial least squares discriminant analysis (PLS-DA) of LA-ICP-MS data for scheelite from orogenic gold and intrusion-intrusion related gold deposits (from Sciuba et al. 2020 and De Bronac de Vazelhes et al. 2021; ESM1 Table S6) and skarn systems (this study). **a.** qw*1–qw*2 (first and second loadings) plot showing the correlations among elemental variables and different deposit types. **b.** t1–t2 (first and second scores) plot showing the distribution of scheelite analyses in the latent variable space defined by qw*1–qw*2. Note that qw*1 separates fluid origin whereas qw*2 separates oxygen fugacity. **c.** The Variable Importance on Projection (VIP) plot shows the importance of compositional variables in classification of the model

is a considerable overlap. Sciuba et al. (2020) showed that multivariate statistical methods (PLS-DA) allow better discrimination of scheelite from magmatic-hydrothermal systems from those from orogenic gold deposits.

A PLS-DA of LA-ICP-MS scheelite composition from this study and literature ($n = 711$ in total) using 18 elements, ΣREE and Eu anomaly, is applied to compare scheelite composition from intrusion related gold, orogenic gold, reduced skarn, and oxidized skarn deposits (Fig. 14). Other deposit types in our sample suite had insufficient data to be included in this PLS-DA. Figure 14a shows that orogenic gold deposits plot at negative qw*1 and qw*2, as result of the Sr, Pb, Na, Ba, and Eu anomaly correlation. An intrusion-related gold deposit (Crusader deposit) plots at negative qw*1 and positive qw*2 due to correlated As and V, and oxidized skarn deposits plot

at positive qw*1 and qw*2, as it correlates with Ti and Mo (Fig. 14a). Reduced skarns deposits plot at positive qw*1 and negative qw*2 due to correlation of Nb and Mn. Overall, reduced skarn, and oxidized skarn deposits from intrusion-related gold, oxidized and reduced skarns deposits by qw*1.

Figure 14b shows that scheelite from orogenic gold deposits forms a cluster at negative t1 due to high Sr and Pb concentrations, but also scatters from negative and positive t2 because of high Y and As concentrations, respectively (Fig. 14a–b). Scheelite from oxidized skarns plots mostly at positive t1 and t2 due to high Mo content, but few analyses have negative t2. Reduced skarn scheelite plots at positive t1 and negative t2 due to high contents of Nb and Mn. Some of the analyses of reduced skarn scheelite plot at positive t1 and overlap with scheelite from oxidized skarns. Scheelite

from intrusion-related gold deposit forms a cluster in negative t1 and positive t2 due to high As and V concentrations.

The high Sr concentration in scheelite from orogenic gold deposit is likely because of higher content of Sr in hydrothermal fluids derived from dehydration of metasediments and/or mafic–ultramafic volcanic rocks associated with orogenic gold deposits (Kempe et al. 2006; Poulin et al. 2018; Sciuba et al. 2020). Given that Sr is compatible during fractional crystallization, scheelite crystalized from fluids exsolved from felsic magmas has low Sr concentration (<< 1000 ppm, Poulin et al. 2018). High Nb, Ta, and Mo contents characterize scheelite formed from fluids exsolved from felsic magmas (Fig. 14a–b) due to the incompatibly of these elements during fractional crystallization and to higher fO_2 of magmatic-hydrothermal, relative to metamorphic fluids. Given that Sr and Pb are negatively correlated with Mo, Nb, and Ta, qw*1 allows discrimination of scheelite formed from distinct hydrothermal fluid sources, i.e., metamorphic vs magmatic. High As and V concentrations characterize the intrusion-related deposit (Crusader gold deposit; Sciuba et al. 2020)

and oxidized skarns (this study), and Mn characterizes scheelite from more reduced environments. The negative correlation between As–V and Mn in qw*2 discriminates scheelite crystallized from contrasting fO_2 (Fig. 14a–b).

Given that Mo and Sr are the main elements used for discriminating the source of hydrothermal fluids (Fig. 14a) and because Mo and Sr are commonly analyzed, we propose that, although there are some overlaps, the relation between these elements can be used to discriminate scheelite derived from metamorphic and magmatic fluids (Fig. 15). Scheelite from magmatic-hydrothermal settings such as intrusion-related gold, oxidized and reduced skarns, Sn–W quartz-veins/greisen, and Mo–W porphyry deposits have high Mo, and low to intermediate Sr concentrations (Fig. 15), as does scheelite associated with VMS hydrothermal deposits. Similar to scheelite associated with orogenic gold deposits, metamorphic scheelite from W occurrence in metasediments has low Mo and intermediate to high Sr contents. The Mo and Sr correlation does not discriminate scheelite from different magmatic-hydrothermal deposits, however, reinforcing the advantage of PLS-DA.
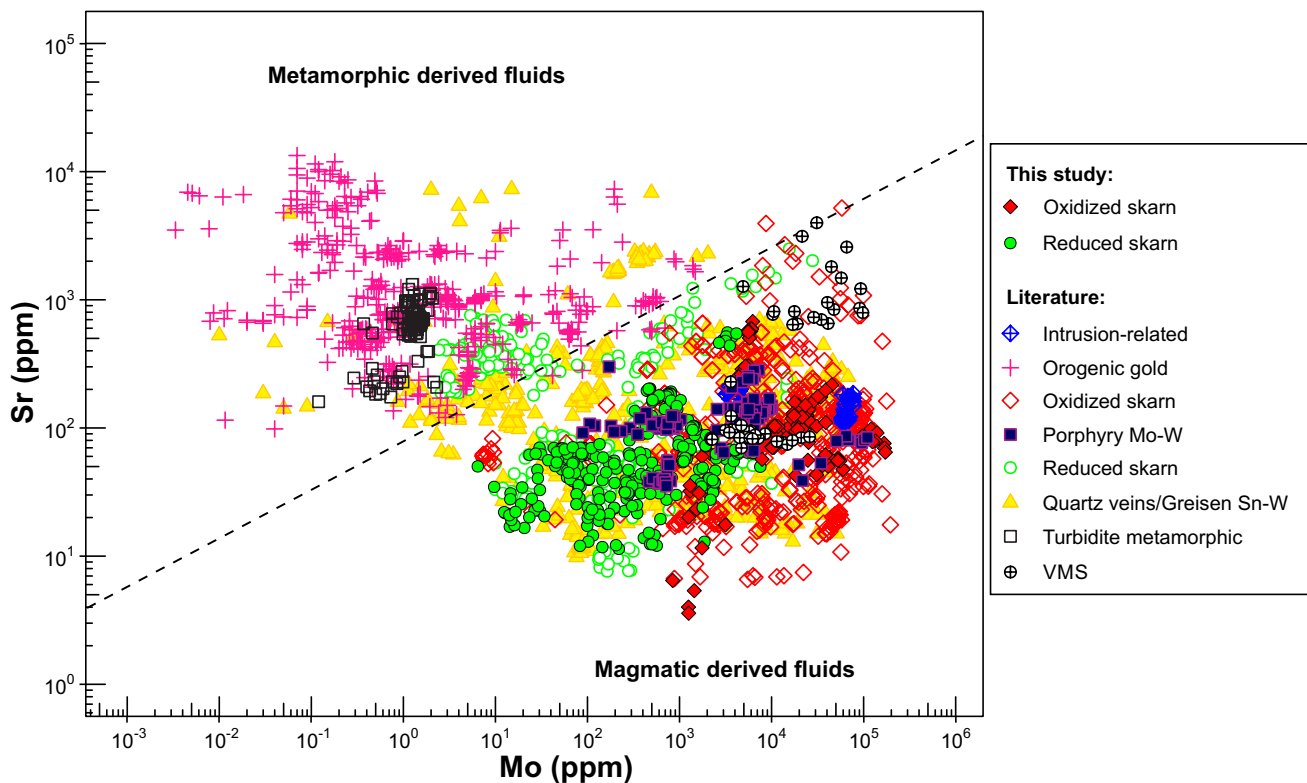

Fig. 15 Binary plot of Mo versus Sr showing that scheelite formed from metamorphic fluids can be discriminated from that of magmatic derived fluids due to lower Mo and higher Sr concentrations. Data from: Song et al. (2014), Fu et al. (2016), Guo et al. (2016), Poulin (2016), Sun and Chen (2017), Cave et al. (2017), Plotinskaya et al. (2017), Li et al. (2018,2019), Ding et al. (2018), Song et al. (2019), Zang and Gao (2018), Zhao et al. (2018), Liu et al. (2019), Wu et al. (2019), Xu et al. (2019), Yuan et al (2019), Chen et al. (2020), Sciuba et al. (2020), Seo et al. (2020), Su et al. (2020), and de Bronac de Vazelles et al. (2021)

Conclusions

This work shows the efficiency of scheelite chemical composition as a tool for mineral exploration targeting. Texturally, scheelite may display complex zoning patterns and dissolution front textures, which indicate changes in physicochemical conditions of hydrothermal fluids during scheelite crystallization. Skarn prograde scheelite is zoned, whereas retrograde scheelite is commonly homogeneous in CL and BSE images. The trace element composition of scheelite reflects compositional features inherited from the magmatic-derived fluids and the nature of co-precipitated minerals. Scheelite displays five main REE patterns with positive and negative Eu anomalies: steep and shallow negative slopes, concave, flat to concave and convex shapes. These different REE patterns reflect differences in salinity of hydrothermal fluids, type of co-precipitating minerals, and amount of early scheelite precipitation. Niobium, Ta, Mn, Mo, V, and As are the best elements to discriminate scheelite according to redox skarn types, felsic intrusion composition, and metal association. High Mo, As, and V contents characterize scheelite from oxidized skarns, metaluminous felsic intrusions, Cu-polymetallic, W–Mo(Sn), and W deposits. High Mn, Nb, and Ta concentrations are typically of scheelite from reduced skarns, peralunimous felsic intrusions, W–Au, and W–Cu deposits. The PLS-DA results show that scheelite from magmatic-hydrothermal settings can be discriminated from those from orogenic gold deposits due to higher Mo, Nb, and, Ta and lower Sr abundances. Overall, our results support the use of scheelite as an indicator mineral for exploration targeting.

Declarations

Conflict of interest The authors declare no competing interests.

References

Aitchison J (1986) The statistical analysis of compositional data. (C a Hall, Ed) London.

Andersson S, Wagner T, Jonsson E, Fusswinkel T, Whitehouse M (2019) Apatite as a tracer of the source, chemistry and evolution of ore-forming fluids: the case of the Olserum-Djupedal REE-phosphate mineralization, SE Sweden. Geochim Cosmochim Acta 255:163–187

Averill S (2001) The application of heavy indicator mineralogy in mineral exploration with emphasis on base metal indicators in glaciated metamorphic and plutonic terrains. Geol Soc London, Spec Publ 185:69–81

Ayers JC, Watson EB (1993) Rutile solubility and mobility in supercritical fluids. Contrib Mineral Petrol 114:321–330

Baker T, Achterberg EV, Ryan CG, Lang JR (2004) Composition and evolution of ore fluids in a magmatic-hydrothermal skarn deposit. Geology 32(2):117–120

Baker JM, Wilkinson JJ, Wilkinson CC, Cooke DR, Ireland T (2020) Epidote trace element chemistry as an exploration tool in the Collahuasi District. Northern Chile Econ Geol 115(4):749–770

Bau M (1991) Rare earth element mobility during hydrothermal and metamorphic fluid-rock interaction and the significance of the oxidation state of europium. Chem Geol 93:219–230

Boutroy E, Dare S, Beaudoin G, Barnes S-J, Lightfoot P (2014) Magnetite composition in Ni-Cu-PGE deposits worldwide and its application to mineral exploration. J Geochem Explor 145:64–81

Bromiley GD (2021) Do concentrations of Mn, Eu and Ce in apatite reliably record oxygen fugacity in magmas? Lithos 384–385:105900

Brown I, Nesbitt B (1987) Gold-copper-bismuth mineralization in hedenbergitic skarn, Tombstone Mountains, Yukon. Can J Earth Sci 24:2362–2372

Brown VS, Baker T, Stephens JR (2002) Ray Gulch tungsten skarn, Dublin Gulch, central Yukon: Gold-tungsten relationships in intrusion-related ore systems and implications for gold exploration. In: Yukon exploration and geology 2001, DS Emond, LH Weston and LL Lewis (eds), Exploration and Geological Services Division, Yukon Region, Indian and Northern Affairs Canada, p 259–268

Brugger J, Giere R, Grobety B, Uspensky E (1998) Scheelite-powellite and paraniite-(Y) from the Fe-Mn deposit at Fianel, Eastern Swiss Alps. Am Mineral 83:1100–1110

Brugger J, Lahaye Y, Costa S, Lambert D, Bateman R (2000) Inhomogeneous distribution of REE in scheelite and dynamics of Archaean hydrothermal systems (Mt Charlotte and Drysdale gold deposits, Western Australia). Contrib Mineral Petrol 139:251–264

Brugger J, Etschmann B, Pownceby M, Liu W, Grundler P, Brewe D (2008) Oxidation state of europium in scheelite: tracking fluid–rock interaction in gold deposits. Chem Geol 257:26–33

Brugger J, Liu W, Etschmann B, Mei Y, Sherman DM, Testemal D (2016) A review of the coordination chemistry of hydrothermal systems, or do coordination changes make ore deposits? Chem Geol 447:219–253

Burt D (1989) Compositional and phase relations among rare earth elements. Rev Mineral 21:259–307

Chang Z, Shu Q, Meinert L, (2019) Skarn deposits of China. In: Chang, Zhaoshan, and Goldfard, Richard J (ed) Mineral deposits of China. Special Publications of the Society of Economic Geologists, 22 Society of Economic Geologists, Littleton, CO, USA, pp 189–234

Choi W, Park C, Song Y (2020) Multistage W-mineralization and magmatic-hydrothermal fluid evolution: microtextural

and geochemical footprints in scheelite from the Weondong W-skarn deposit. South Korea Ore Geol Rev 116:103219

Cooke DR, Wilkinson JJ, Baker M, Agnew P, Phillips J, Chang Z, Chen H, Wilkinson CC, Inglis S, Hollings P, Zhang L, Gemmell B, White NC, Danyushevsky L, Martin H (2020) Using mineral chemistry to aid exploration: a case study from the resolution porphyry Cu-Mo deposit. Arizona Eco Geol 115(4):813–840

Cook N, Ciobanu CL, George L, Zhu Z-Y, Wade B, Ehrig K (2016) Trace element analysis of minerals in magmatic-hydrothermal ores by laser ablation inductively-coupled plasma mass spectrometry: approaches and opportunities. Minerals 6(4):111

Dare SAS, Barnes SJ, Beaudoin G, Méric J, Boutroy E, Potvin-Doucet C (2014) Trace elements in magnetite as petrogenetic indicators. Mineral Deposita 49:785–796

Dare SAS, Barnes SJ, Beaudoin G (2012) Variation in trace element content of magnetite crystallized from a fractionating sulfide liquid, Sudbury, Canada: implications for provenance discrimination. Geochim Cosmochim Acta 88:27–50

de Bronac de Vazelhes V, Beaudoin G, McMartin I, Côté-Mantha O, Boulianne-Verschelden N (2021) Assessment of the Amaruq gold deposit signature in glacial sediments using multivariate geochemical data analysis and indicator minerals. J Geochem Explor 228:106800

Dick L, Hodgson C (1982) The MacTung W-Cu(Zn) contact metasomatic and related deposits of the northeastern Canadian Cordillera. Econ Geol 77:845–867

Dostal J, Kontak D, Chatterjee A (2009) Trace element geochemistry of scheelite and rutile from metaturbidite-hosted quartz vein gold deposits, Meguma Terrane, Nova Scotia, Canada: genetic implications. Mineral Petrol 97:95–109

Drake MJ, Weill DF (1975) Partition of Sr, Ba, Ca, Y, Eu2+, Eu3+, and other REE between plagioclase feldspar and magmatic liquid: an experimental study. Geochim Cosmochim Acta 39:689–712

Dupuis C, Beaudoin G (2011) Discriminant Diagrams for Iron-Oxide Trace Element Fingerprinting of Mineral Deposit Types Mineral Deposita 46:319–335

Duran C, Barnes S-J, Corkerybc J (2016) Trace element distribution in primary sulfides and Fe–Ti oxides from the sulfide-rich pods of the Lac des Iles Pd deposits, Western Ontario, Canada: constraints on processes controlling the composition of the ore and the use of pentlandite compositions. J Geochem Explor 166:45–63

Duran C, Dubé-Loubert H, Page P, Barnes S-J, Roy M, Savard D, Cave BJ, Arguin J-P, Mansur E (2019) Applications of trace element chemistry of pyrite and chalcopyrite in glacial sediments to mineral exploration targeting: example from the Churchill Province, northern Quebec, Canada. J Geochem Explor 196:105–130

Einaudi M, Burt D (1982) Introduction, terminology, classification, and composition of skarn deposits. Econ Geol 77(4):745–754

Einaudi M, Meinert L, Newberry R (1981) Skarn deposits. Econ Geol 75:317–391

Eppinger, R.G., et al., 2011 Exploration case study using indicator minerals in till at the giant Pebble porphyry Cu-Au-Mo deposit, southwest Alaska, USA, in Indicator mineral methods in mineral exploration: Workshop in the 25th International Applied Geochemistry Symposium 2011, 22–26 August 2011 Rovaniemi, Finland p 41–48 https://pubs.er.usgs.gov/publication/70156777

Eriksson L, Johansson E, Kettaneh-Wold N, Wold S (2001) Multi- and megavariate data analysis, principles and applications. UMETRICS, Umea, 425 p

Fu Y, Sun X, Zhou H, Lin H, Jiang L, Yang T (2017) In-situ LA-ICP-MS trace elements analysis of scheelites from the giant Beiya gold-polymetallic deposit in Yunnan Province, Southwest China and its metallogenic implications. Ore Geol Rev 80:828–837

Gaspar M, Knaack C, Meinert L, Moretti R (2008) REE in skarn systems: a LA-ICP-MS study of garnets. Geochim Cosmochim Acta 72:185–205

George L, Cook N, Ciobanu C, Wade B (2015) Trace and minor elements in galena: a reconnaissance LA-ICP-MS study. Am Mineral 100:548–569

George L, Cook N, Crowe B, Ciobanu C (2018) Trace elements in hydrothermal chalcopyrite. Mineral Mag 82(1):59–88

Ghaderi M, Palin J, Campbell I, Sylvester P (1999) Rare earth element systematics in scheelite from hydrothermal gold deposits in the Kalgoorlie-Norseman region, Western Australia. Econ Geol 94:423–437

Gregory DD, Cracknell MJ, Large RR, McGoldrick P, Kuhn S, Maslennikov VV, Baker MJ, Fox N, Belousov I, Figueroa MC, Steadman JA, Fabris AJ, Lyons TW (2019) Distinguishing ore deposit type and barren sedimentary pyrite using laser ablation-inductively coupled plasma-mass spectrometry trace element data and statistical analysis of large data sets. Econ Geol 114(4):771–786

Grütter HS, Gurney JJ, Menzies AH, Winter F (2004) An updated classification scheme for mantle-derived garnet, for use by diamond explorers. Lithos 77:841–857. https://doi.org/10.1016/jlithos200 404012

Grzela D, Beaudoin G, Bédard É (2019) Tourmaline, scheelite, and magnetite compositions from orogenic gold deposits and glacial sediments of the Val-d'Or district (Québec, Canada): applications to mineral exploration. J Geochem Explor 206:106355

Guo Z, Li J, Xu X, Song Z, Dong X, Tian J, Yang Y, She H, Xiang A, Kang Y (2016) Sm/Nd dating and REE composition of scheelite for the Honghuaerji scheelite deposit, Inner Mongolia, Northeast China. Lithos 261:307–321

Gurney JJ, Zweistra P (1995) The interpretation of the major element compositions of mantle minerals in diamond exploration. J Geochem Explor 53:293–309

Haas J, Shock EL, Sassani D (1995) Rare earth elements in hydrothermal systems: estimates of standard partial molal thermodynamic properties of aqueous complexes of the rare earth elements at high. Geochim Cosmochim Acta 59:4329–4350

Han J, Chen H, Hing C, Hollings P, Chu G, Zang L, Sun S (2020) Texture and geochemistry of multi-stage hydrothermal scheelite in the Tongshankou porphyry-skarn Cu-Mo(-W) deposit, eastern China: implications for ore-forming process and fluid metasomatism. Am Mineral 105:945–954

Hart C (2007) Reduced Intrusion-Related Gold Systems. In W D Goodfellow, Mineral Deposits of Canada: a synthesis of major deposit-types, district metallogeny, the evolution of geological provinces, and exploration methods (pp 95–112) Geological Association of Canada, Mineral Deposits Division

Hsu L (1977) Effects of oxygen and sulfur fugacities on the scheelite-tungstenite and powellite-molybdenite stability relations. Econ Geol 72:664–670

Huang X-W, Boutroy E, Makvandi S, Beaudoin G, Corriveau L, De Toni A (2019) Trace element composition of iron oxides from IOCG and IOA deposits: relationship to hydrothermal alteration and deposit subtypes. Mineral Deposita 54:525–552

Ishihara S (1981) The magnetite-series and ilmenite-series granitic rocks. Min Geol 27:293–305

Ismail R, Ciobanu CL, Cook NJ, Teale GS, Giles D, Mumm AS, Wade B (2014) Rare earths and other trace elements in minerals from skarn assemblages, Hillside iron oxide–copper–gold deposit, Yorke Peninsula, South Australia. Lithos 184:456–477

James-Smith J, Cauzid J, Testemale D, Liu W, Hazemann J, Proux O, Etschmann B, Philippot P, Banks D, Williams P, Brugger J (2010) Arsenic speciation in fluid inclusions using micro-beam X-ray absorption spectroscopy. Am Mineral 95(7):921–932

Jochum KP, Nohl U, Herwig K, Lammel E, Hofmann SB, AW, (2005) GeoReM: a new geochemical database for reference materials and isotopic standards. Geostand Geoanal Res 29:333–338

Kelley KD et al (2011) Porphyry Cu indicator minerals in till as an exploration tool: example from the giant Pebble porphyry Cu-Au-Mo deposit. Alaska, USA, Geochemistry: Exploration, Environment, Analysis 11(4):321. https://doi.org/10.1144/1467-7873/10-IM-041

Kempe U, Belyatsky B, Krymsky R, Kremenetsky A, PA I, (2001) Sm-Nd and Sr isotope systematics of scheelite from the giant Au(-W) deposit Muruntau (Uzbekistan): implications for the age and sources of Au mineralization. Mineral Deposita 36:379–392

Kwak T, Tan T (1981) The geochemistry of zoning in the skarn minerals at the King Island Dolphin mine. Econ Geol 76:468–497

Li J, Li X, Xiao R (2019) Multiple-stage tungsten mineralization in the Silurian Jiepai W skarn deposit, South China: insights from cathodoluminescence images, trace elements, and fluid inclusions of scheelite. J Asian Earth Sci 181:103898

Liu H, Beaudoin G (2021) Geochemical signatures in native gold derived from Au-bearing ore deposits. Ore Geol Rev 132:104066

Liu J, Li W, Zhu X, Li C, Zhou Q, Yang F (2020) Origin and evolution of ore-forming fluids of the Larong W-(Mo) deposit, eastern Tibet: constraints from fluid inclusions, H-O isotopes, and scheelite geochemistry. Ore Geol Rev 124:103620

Lu H-Z, Liu Y, Wang C, Xu Y, Li H (2003) Mineralization and fluid inclusion study of the Shizhuyuan W-Sn-Bi-Mo-F skarn deposit, Hunan Province, China. Econ Geol 98:955–974

Mair J, Goldfarb R, Johnson C, Hart C, Marsh E (2006) Geochemical constraints on the genesis of the Scheelite Dome intrusion-related gold deposit, Tombstone gold belt, Yukon, Canada. Econ Geol 101:523–553

Makvandi S, Ghasemzadeh-Barvarz M, Beaudion G, Grunsky E, McClenaghan M, Duchesne C (2016a) Principal component analysis of magnetite composition from volcanogenic massive sulfide deposits: case studies from the Izok Lake (Nunavut, Canada) and Halfmile Lake (New Brunswick, Canada) deposits. Ore Geol Rev 72:60–85

Makvandi S, Ghasemzadeh-Barvarz M, Beaudion G, Grunsky EC, McClenaghan MB, Duchesne C (2016b) Partial least squares discriminant analysis of trace element compositions of magnetite from various VMS deposit subtypes: application to mineral exploration. Ore Geol Rev 78:388–408

Makvandi S, Huang X, Beaudoin G, Quirt D, Ledru P, Fayek M (2020) Trace element signatures in hematite and goethite associated with the Kiggavik-Andrew Lake structural trend U deposits (Nuvanut, Canada). Mineral Deposita 56:509–535

Manéglia N, Beaudoin G, Simard M (2017) Indicator minerals of the Meliadine orogenic gold deposits, Nunavut (Canada), and application to till surveys. Geochem Explor Environ Anal 18:241–251

Mansur ET, Barnes S-J, Duran C (2021) An overview of chalcophile element contents of pyrrhotite, pentlandite, chalcopyrite, and pyrite from magmatic Ni-Cu-PGE sulfide deposits. Mineral Deposita 56:179–204

Mao M, Rukhlov A, Rowins S, Spence J, Coogan L (2016) Apatite trace element compositions: a robust new tool for mineral exploration. Econ Geol 111:1187–1222

Mathieson G, Clark A (1984) The Cantung E Zone scheelite skarn orebody, Tungsten Northwest Territories: a revised genetic model. Econ Geol 79:883–901

McClenaghan M (2005) Indicator mineral methods in mineral exploration. Geochem Explor Environ Anal 5(3):233–245

McClenaghan M, Parkhill M, Pronk A, Seaman A, McCurdy M, Leybourne M (2017) Indicator mineral and geochemical signatures associated with the Sisson W-Mo deposit, New Brunswick, Canada. Geochem Explor Environ Anal 17:297–313

Meinert L (1997) Application of skarn deposit zonation models to mineral exploration. Explor Mining Geol 6(2):185–208

Meinert L, Dipple G, Nicolescu S (2005) World skarn deposits. In: Hedenquist J, Thompson J, Goldfarb R, Richards J (eds) Econ Geol 100th Anniversary Volume. Society of Economic Geologists, Littleton, CO, pp 299–336

Migdisov A, Williams-Jones AE, Brugger J, Caporuscio F (2016) Hydrothermal transport, deposition, and fractionation of REE: experimental data and thermodynamic calculations. Chem Geol 439:13–42

McDonough WF, Sun SS (1995) The composition of the earth. Chem Geol 120:223–253

Nassau K (1963) Calcium tungstate—IV: the theory of coupled substitution. J of Physics and Chemistry of Solids 24:1511–2151

Newberry R (1982) Tungsten-bearing skarns of the Sierra Nevada I The Pine Creek Mine, California. Econ Geol 77:823–844

Newberry R (1983) The formation of subcalcic garnet in scheelite-bearing skarns. Can Mineral 21:529–544

Newberry R, Swanson S (1986) Scheelite skarn granitoids: an evaluation of the roles of magmatic source and process. Ore Geol Rev 1:57–81

O'Brien J, Spry P, Teale G, Jackson S, Koenig A (2015) Gahnite composition as a means to fingerprint metamorphosed massive sulfide and non-sulfide zinc deposits. J Geochem Explor 159:48–61

Palarea-Albaladejo J, Martín-Fernández JA (2013) Values below detection limit in compositional chemical data. Anal Chim Acta 764:32–43

Palarea-Albaladejo J, Martín-Fernández J (2015) zCompositions—R package for multivariate imputation of left-censored data under a compositional approach. Chemometr Intell Lab Syst 143:85–96

Pan X, Hou Z, Zhao M, Li Y, Ouyang Y, Wei J, Yang Y (2020) Fluid inclusion and stable isotope constraints on the genesis of the worldclass Zhuxi W(Cu) skarn deposit in South China. J Asian Earth Sci 190:104192

Paton, C, Hellstrom, J, Paul, B, Woodhead, J, and Hergt, J., 2011, Iolite: freeware for the visualization and processing of mass spectrometric data: Journal of Analytical Atomic Spectrometry, v. 26, p. 2508–2518. https://doi.org/10.1039/c1ja10172b

Poitrenaud T, Poujoi M, Augier R, Marcoux E (2019) The polyphase evolution of a late Variscan W/Au deposit (Salau, French Pyrenees): insights from REE and U/Pb LA-ICP-MS analyses. Mineral Deposita 55:1127–1147

Plotinskayaa O, Baksheevb I, Minervina EA (2018) REE distribution in scheelite from the Yubileinoe porphyry gold deposit, South Urals: evidence from LA-ICP-MS Data. Geol Ore Depos 60(4):355–364

Porter JP (2013) Source, emplacement and evolution of the Morgan Creek Pluton, Sierra Nevada Batholith, California, USA PhD thesis, Salt Lake City, USA, The University of Utah, 201 p.

Porter J, McNaughtona N, Evansa N, McDonald J (2020) Rutile as a pathfinder for metals exploration. Ore Geol Rev 120:03406

Poulin R, Kontak D, McDonald A, McClenaghan M (2018) Assessing scheelite as an ore-deposit discriminator using its trace element and REE chemistry. Can Mineral 56:265–302

Purtov VK, KoteVnikova AL (1993) Solubility of titanium in chloride and fluoride hydrothermal solutions. Intern Geol Rev 35:3279–3287

R Core Team (2021). R: a language and environment for statistical computing. R Foundation for Statistical Computing, Vienna, Austria. URL https://www.R-project.org/.

Raimbault L, Baumer A, Dubru M, Benkerrou C, Croze V, Zahm A (1993) REE fractionation between scheelite and apatite in hydrothermal conditions. Am Mineral 78:1275–1285

Roberts S, Palmer M, Waller L (2006) Sm-Nd and REE characteristics of tourmaline and scheelite from the Bjorkdal gold deposit,

northern Sweden: evidence of an intrusion-related gold deposit? Econ Geol 101(7):1415–1425

Rottier B, Casanova V (2020) Trace element composition of quartz from porphyry systems: a tracer of the mineralizing fluid evolution. Miner Deposita 55:843–862

Sciuba M, Beaudoin G, Grzela D, Makvandi S (2020) Trace element composition of scheelite in orogenic gold deposits. Miner Deposita 55:1149–1172

Shannon RD (1976) Revised effective ionic radii and systematic studies of interatomic distances in halides and chalcogenides. Acta Cryst A 32:751–767

Seo J, Yoo B, Yang Y (2020) Scheelite geochemistry of the Sangdong W-Mo deposit and W prospects in the southern Taebaeksan metallogenic region. Korea Geosci J 24:701–721

Shu Q, Chang Z, Lai Y, Hu X, Wu H, Zhang Y, Wang P, Zhai D, Zhang C (2019) Zircon trace elements and magma fertility: insights from porphyry (-skarn) Mo deposits in NE China. Miner Deposita 54:645–656

Singoyi B, Zaw K (2001) A petrological and fluid inclusion study of magnetite–scheelite skarn mineralization at Kara, Northwestern Tasmania: implications for ore genesis. Chem Geol 173:239–253

Soloviev S (2015) Geology, mineralization, and fluid inclusion characteristics of the Kumbel oxidized W-Cu-Mo skarn and Au-W stockwork deposit, Tien-Shan, Kyrgyzstan. Mineral Deposita 50:187–220

Soloviev S, Kryazhev SG, Dvurechenskaya SS (2015) Geology, mineralization, and fluid inclusion characteristics of the Lermontovskoe reduced-type tungsten (±Cu, Au, Bi) skarn deposit, Sikhote-Alin, Russia. Ore Geol Rev 89:15–39

Soloviev S, Kryazhev S, Dvurechenskaya S (2017) Geology, mineralization, stable isotope, and fluid inclusion characteristics of the Vostok-2 reduced W-Cu skarn and Au-W-Bi-As stockwork deposit, Sikhote-Alin, Russia. Ore Geol Rev 86:338–365

Song G, Qin K, Li G, Evans N, Chen L (2014) Scheelite elemental and isotopic signatures: Implications for the genesis of skarn-type W-Mo deposits in the Chizhou area, Anhui Province Eastern China. Am Mineral 99:303–317

Song G, Cook NJ, Li G, Qin K, Ciobanu CL, Yang Y, Xu Y (2019) Scheelite geochemistry in porphyry-skarn W-Mo systems: a case study from the Gaojiabang Deposit. East China Ore Geol Rev 113:103084

Souza Neto JA, Legrand JM, Volfinger M, Pascal M-L, Sonnet P (2008) W-Au skarns in the Neo-Proterozoic Seridó Mobile Belt, Borborema Province in northeastern Brazil: an overview with emphasis on the Bonfim deposit. Miner Deposita 43:185–205

Su Q, Mao J, Sun J, Zhao L, Xu S (2020) Geochemistry and origin of scheelites from the Xiaoyao tungsten skarn deposit in the Jiangnan Tungsten Belt. SE China Minerals 10:271

Su Q, Mao J, Wu S, Zhang Z, Xu S (2018) Geochronology and geochemistry of the granitoids and re-forming age in the Xiaoyao tungsten polymetallic skarn deposit in the Jiangnan Massif tungsten belt China: implications for their petrogenesis, geodynamic setting, and mineralization. Lithos 29:365–381

Sun K, Chen B (2017) Trace elements and Sr-Nd isotopes of scheelite: Implications for the W-Cu-Mo polymetallic mineralization of the Shimensi Deposit, south China. Am Mineral 102:1114–1128

Sun K, Chen B, Deng J (2019) Ore genesis of the Zhuxi supergiant W-Cu skarn polymetallic deposit, South China: evidence from scheelite geochemistry. Ore Geol Rev 107:14–29

Sverjensky D (1984) Europium redox equilibria in aqueous solution. Earth Planet Sci Lett 67:70–78

Sylvester PJ, Jackson SE (2016) A brief history of laser ablation inductively coupled plasma mass spectrometry (LA–ICP–MS). Elements 12(5):307–310

Testemale D, Hazemann JL, Pokrovski GS, Joly Y, Roux J, Argoud R, Geaymond O (2004) Structural and electronic evolution of the As(OH)3 molecule in high temperature aqueous solutions: an X-ray absorption investigation. J Chem Phys 121(18):8973–8982

Thompson J, Sillitoe R, Baker T, Lang J, Mortensen J (1999) Intrusion-related gold deposits associated with tungsten-tin provinces. Miner Deposita 34(4):323–334

Tian Y, Etschmann B, Mei Y, Grundler PV, Testemale D, Hazemann J-L, Elliott P, Ngothai Y, Brugger J (2014) Speciation and thermodynamic properties of manganese(II) chloride complexes in hydrothermal fluids: in situ XAS study. Geochim Cosmochim Acta 129:77–95

Toverud O (1984) Dispersal of tungsten in glacial drift and humus in Bergslagen, southern central Sweden. J Geochem Explor 21:261–272

Uspensky E, Brugger J, Graeser S (1998) REE geochemistry systematics of scheelite from the Alps using luminescence spectroscopy: from global regularities to facies control. Schweiz Mineral Petrogr Mitt 78:33–56

Wilkinson J, Chang Z, Cooke D, Baker M, Wilkinson C, Inglis S, Gemmell J (2015) The chlorite proximitor: a new tool for detecting porphyry ore deposits. J Geochem Explor 152:10–26

Wilkinson J, Baker M, Cooke D, Wilkinson C (2020) Exploration targeting in porphyry Cu systems using propylitic mineral chemistry. Econ Geol 115:771–791

Wintzer NE (2019) Geology, geochronology, and geochemistry of the stibnite-yellow pine gold-antimony-tungsten mining area, Idaho. PhD thesis, Pullman, USA Washington State University 297p

Wu S, Mao J, Ireland T, Zaho Z, Yao F, Yang Y, Sun W (2019) Comparative geochemical study of scheelite from the Shizhuyuan and Xianglushan tungsten skarn deposits, South China: implications for scheelite mineralization. Ore Geol Rev 109:448–464

Xu J, Ciobanu C, Cook NC, Slattery A (2020) Crystals from the powellite-scheelite series at the nanoscale: a case study from the Zhibula Cu skarn, Gangdese Belt. Tibet Minerals 9:340

Yuan L, Chi G, Wang M, Li Z, Xu D, Deng T, Geng J, Hu M, Zhang L (2019) Characteristics of REEs and trace elements in scheelite from the Zhuxi W deposit, South China: implications for the ore-forming conditions and processes. Ore Geol Rev 109:585–597

Zang Z, Xie G, Mao J, Liu W, Olin P, Li W (2019) Sm-Nd dating and in-situ LA-ICP-MS trace element analyses of scheelite from the Longshan Sb-Au deposit, Xiangzhong metallogenic province. South China Minerals 9:87

Zaw K, Singoyi B (2000) Formation of magnetite-scheelite skarn mineralization at Kara, Northwestern Tasmania: evidence from mineral chemistry and stable isotopes. Econ Geol 95:1215–1230

Zhang Q, Zhang RQ, Gao JF, Lu JJ, Wu JW (2018) In-situ LA-ICP-MS trace element analyses of scheelite and wolframite: constraints on the genesis of veinlet-disseminated and vein-type tungsten deposits, South China. Ore Geol Rev 99:166–179

Zhao W, Zhou M-F, Williams-Jones A, Zhao Z (2018) Constraints on the uptake of REE by scheelite in the Baoshan tungsten skarn deposit, South China. Chem Geol 477:123–136

Zheng W, Tang J, Zhong K, Ying L, Leng Q, Ding S, Lin B (2016) Geology of the Jiama porphyry copper–polymetallic system, Lhasa Region, China. Ore Geol Rev 74:151–169